



<b>Publication Year</b>	2017
<b>Acceptance in OA @INAF</b>	2021-01-05T15:19:02Z
<b>Title</b>	The GAPS Programme with HARPS-N at TNG. XIII. The orbital obliquity of three close-in massive planets hosted by dwarf K-type stars: WASP-43, HAT-P-20 and Qatar-2
<b>Authors</b>	Esposito, M.; COVINO, Elvira; DESIDERA, Silvano; Mancini, L.; NASCIMBENI, VALERIO; et al.
<b>DOI</b>	10.1051/0004-6361/201629720
<b>Handle</b>	<a href="http://hdl.handle.net/20.500.12386/29495">http://hdl.handle.net/20.500.12386/29495</a>
<b>Journal</b>	ASTRONOMY & ASTROPHYSICS
<b>Number</b>	601

## The GAPS Programme with HARPS-N at TNG

### XIII. The orbital obliquity of three close-in massive planets hosted by dwarf K-type stars: WASP-43, HAT-P-20 and Qatar-2<sup>★,★★</sup>

M. Esposito<sup>1</sup>, E. Covino<sup>1</sup>, S. Desidera<sup>2</sup>, L. Mancini<sup>16,3,6</sup>, V. Nascimbeni<sup>10,2</sup>, R. Zanmar Sanchez<sup>4</sup>, K. Biazzo<sup>4</sup>, A. F. Lanza<sup>4</sup>, G. Leto<sup>4</sup>, J. Southworth<sup>5</sup>, A. S. Bonomo<sup>6</sup>, A. Suárez Mascareño<sup>7,8</sup>, C. Boccato<sup>2</sup>, R. Cosentino<sup>11</sup>, R. U. Claudi<sup>2</sup>, R. Gratton<sup>2</sup>, A. Maggio<sup>9</sup>, G. Micela<sup>9</sup>, E. Molinari<sup>11,14</sup>, I. Pagano<sup>4</sup>, G. Piotto<sup>10,2</sup>, E. Poretti<sup>12</sup>, R. Smareglia<sup>13</sup>, A. Sozzetti<sup>6</sup>, L. Affer<sup>9</sup>, D. R. Anderson<sup>5</sup>, G. Andreuzzi<sup>11,15</sup>, S. Benatti<sup>2</sup>, A. Bignamini<sup>13</sup>, F. Borsa<sup>12</sup>, L. Borsato<sup>10,2</sup>, S. Ciceri<sup>3</sup>, M. Damasso<sup>6</sup>, L. di Fabrizio<sup>11</sup>, P. Giacobbe<sup>6</sup>, V. Granata<sup>10,2</sup>, A. Harutyunyan<sup>11</sup>, T. Henning<sup>3</sup>, L. Malavolta<sup>10,2</sup>, J. Maldonado<sup>9</sup>, A. Martinez Fiorenzano<sup>11</sup>, S. Masiero<sup>2</sup>, P. Molaro<sup>13</sup>, M. Molinaro<sup>13</sup>, M. Pedani<sup>11</sup>, M. Rainer<sup>12</sup>, G. Scandariato<sup>4</sup>, and O. D. Turner<sup>5</sup>

(Affiliations can be found after the references)

Received 14 September 2016 / Accepted 8 February 2017

#### ABSTRACT

**Context.** The orbital obliquity of planets with respect to the rotational axis of their host stars is a relevant parameter for the characterization of the global architecture of planetary systems and a key observational constraint to discriminate between different scenarios proposed to explain the existence of close-in giant planets.

**Aims.** In the framework of the GAPS project, we conduct an observational programme aimed at determining the orbital obliquity of known transiting exoplanets. The targets are selected to probe the obliquity against a wide range of stellar and planetary physical parameters.

**Methods.** We exploit high-precision radial velocity (RV) measurements, delivered by the HARPS-N spectrograph at the 3.6 m Telescopio Nazionale Galileo, to measure the Rossiter-McLaughlin (RM) effect in RV time-series bracketing planet transits, and to refine the orbital parameters determinations with out-of-transit RV data. We also analyse new transit light curves obtained with several 1–2 m class telescopes to better constrain the physical fundamental parameters of the planets and parent stars.

**Results.** We report here on new transit spectroscopic observations for three very massive close-in giant planets: WASP-43 b, HAT-P-20 b and Qatar-2 b ( $M_p = 2.00, 7.22, 2.62 M_J$ ;  $a = 0.015, 0.036, 0.022$  AU, respectively) orbiting dwarf K-type stars with effective temperature well below 5000 K ( $T_{\text{eff}} = 4500 \pm 100, 4595 \pm 45, 4640 \pm 65$  K respectively). These are the coolest stars (except for WASP-80) for which the RM effect has been observed so far. We find  $\lambda = 3.5 \pm 6.8$  deg for WASP-43 b and  $\lambda = -8.0 \pm 6.9$  deg for HAT-P-20 b, while for Qatar-2, our faintest target, the RM effect is only marginally detected, though our best-fit value  $\lambda = 15 \pm 20$  deg is in agreement with a previous determination. In combination with stellar rotational periods derived photometrically, we estimate the true spin-orbit angle, finding that WASP-43 b is aligned while the orbit of HAT-P-20 b presents a small but significant obliquity ( $\Psi = 36^{+10}_{-12}$  deg). By analyzing the CaII H&K chromospheric emission lines for HAT-P-20 and WASP-43, we find evidence for an enhanced level of stellar activity that is possibly induced by star-planet interactions.

**Key words.** planetary systems – stars: individual: WASP-43 – stars: individual: HAT-P-20 – stars: individual: Qatar-2 – techniques: radial velocities – techniques: photometric

## 1. Introduction

The observational study of extrasolar planets flourished in the last two decades and has led to many surprising discoveries that challenged the traditional paradigms of planetary systems formation and evolution. These discoveries reveal that giant planets can exist very close to their parent stars ( $a < 0.1$  AU) and their orbital planes can have large obliquity angles with respect to the host star equatorial planes, at variance with what is seen in our Solar System.

<sup>★</sup> Based on observations collected at the Italian Telescopio Nazionale Galileo (TNG), operated on the island of La Palma by the Fundación Galileo Galilei of the Istituto Nazionale di Astrofisica (INAF) at the Spanish Observatorio del Roque de los Muchachos of the Instituto de Astrofísica de Canarias, in the frame of the programme Global Architecture of Planetary Systems (GAPS).

<sup>★★</sup> Also based on observations collected at the 0.82 m IAC80 Telescope, operated on the island of Tenerife by the Instituto de Astrofísica de Canarias in the Spanish Observatorio del Teide.

Information on the obliquity of exoplanets is more easily accessed when they happen to transit the host star. Several techniques have been exploited to estimate the orbital obliquity of transiting planets (TPs): star spot crossing (Sanchis-Ojeda & Winn 2011; Mancini et al. 2014), asteroseismology (Chaplin et al. 2013), and gravitational darkening (Barnes et al. 2011). However the great majority of the  $\sim 100$  TPs obliquity measurements<sup>1</sup> were obtained by observing the Rossiter-McLaughlin (RM) effect (Rossiter 1924; McLaughlin 1924). The RM effect is an anomaly in the RV orbital trend that occurs during transit, when the planet, by blocking part of the stellar light, causes a distortion of the spectral lines. The shape of the RM anomaly is related to the sky-projected angle  $\lambda$  between the planet orbital axis and the star spin. For a more detailed

<sup>1</sup> We refer to <http://www.astro.keele.ac.uk/jkt/tepcat/rossiter.html> for an updated list of published papers on obliquity measurements.

description of the RM effect see, for example, [Queloz et al. \(2000\)](#), [Ohta et al. \(2005\)](#), [Giménez \(2006\)](#), [Hirano et al. \(2010\)](#), [Boué et al. \(2013\)](#), [Baluev & Shaidulin \(2015\)](#).

Based on about 50 RM measurements, [Albrecht et al. \(2012\)](#); see also [Winn et al. 2010a](#); and [Schlaufman 2010](#)) noticed an empirical  $\lambda$ - $T_{\text{eff}}$  trend: stars with  $T_{\text{eff}} \gtrsim 6250$  K have a broad distribution of obliquities while stars with  $T_{\text{eff}} \lesssim 6250$  K are aligned. Most recent RM measurements have substantially confirmed the trend, even though the transition from aligned to oblique orbits appears to be a smoother function of  $T_{\text{eff}}$ , and some remarkable exceptions have been discovered ([Esposito et al. 2014](#); [Winn et al. 2010b](#)).

The NASA *Kepler* mission has represented a major breakthrough in the field of extrasolar planets science ([Borucki 2016](#)). As of now, the number of *Kepler* candidate transiting planets is larger than 4600 ([Coughlin et al. 2016](#)). Even though the majority of them lack the precise RV follow-up needed for the planet mass determination, they constitute a valuable statistical sample and enable us to infer important general properties of exoplanetary systems. *Kepler* has found that systems with many transiting planets are common ([Lissauer et al. 2011](#)). Simple geometrical considerations lead us to believe that the orbits of these planets must be nearly coplanar; [Fabrycky et al. \(2014\)](#), from the analysis of their transit duration ratios, infer that the statistical mode of the orbital mutual inclinations is in the range 1.0–2.2 deg. On the other hand, [Morton & Winn \(2014\)](#), combining the information on stellar rotational period and projected velocity of 70 *Kepler* objects of interest (KOIs), find with 95% confidence that the obliquities of stars with one transiting planet are systematically larger than those with multiple transiting planets, which suggests that single planets represent dynamically hotter systems than the flat multiple transiting systems. [Mazeh et al. \(2015\)](#) compared the observed amplitude of the rotational photometric modulation of 993 KOIs with 33,614 single *Kepler* stars in the temperature range of 3500–6500 K. They find the amplitudes to be statistically higher for KOIs with  $3500 \text{ K} < T_{\text{eff}} < 6000 \text{ K}$  and lower for  $6000 \text{ K} < T_{\text{eff}} < 6500 \text{ K}$ , and interpret this as an indication that cool TP host stars are aligned, while hot stars tend to have high obliquities. Their result is coherent with what is found using RM measurements.

The attempts to explain the observed obliquity distribution of exoplanets have addressed many fundamental open questions of planet formation and evolution, as well as of physics of star interiors. Do giant planets migrate inward by effect of tidal interaction within the protoplanetary disc ([Lin et al. 1996](#); [Baruteau et al. 2014](#)) or following planet-planet scattering, Kozai-Lidov cycles, and secular chaotic orbital evolution ([Dawson & Murray-Clay 2013](#); [Wu & Lithwick 2011](#))? Are there mechanisms, such as chaotic star formation ([Bate et al. 2010](#); [Thies et al. 2011](#); [Batygin 2012](#)) or stellar internal gravity waves ([Rogers et al. 2012](#)), able to misalign the protoplanetary disc plane and the equatorial stellar plane with respect to each other? How effective are star-planet interactions at re-orientating originally misaligned systems ([Ogilvie 2014](#); [Lai 2012](#))? Theoretical efforts will benefit from the characterization of orbital obliquities in correspondence of a wider range of the relevant parameters, such as orbital separation and eccentricity, star and planet mass, stellar effective temperature and metallicity, etc.

We conduct systematic observations of known transiting planets in the frame of the programme Global Architecture of Planetary Systems (GAPS; [Covino et al. 2013](#); [Desidera et al. 2013](#); [Poretti et al. 2016](#)). The selection of our targets is based on the following criteria: i) we give priority to hot-Jupiter systems that allow us to widen the explored range of stellar

characteristics (i.e., effective temperature and  $\log g$ ) and planet orbital and physical parameters; ii) to guarantee a reliable measurement of the RM effect, we restrict our choice to stars with visual magnitude  $V < 14$  mag. We have already presented measurements of the RM effect for six targets in several papers of the GAPS series: Qatar-1b ([Covino et al. 2013](#)), HAT-P-18b ([Esposito et al. 2014](#)), XO-2b ([Damasso et al. 2015a](#)), KELT-6b ([Damasso et al. 2015b](#)), HAT-P-36b and WASP-11b ([Mancini et al. 2015](#)).

Here we report new observations of the RM effect for three other TPs: WASP-43 b ([Hellier et al. 2011](#)), HAT-P-20 b ([Bakos et al. 2011](#)) and Qatar-2 b ([Bryan et al. 2012](#)). All of them are very massive close-in giant planets (WASP-43 b:  $M_p = 2 M_J$ ,  $a = 0.015$  AU; HAT-P-20 b:  $7.2 M_J$ ,  $0.036$  AU; Qatar-2 b:  $2.6 M_J$ ,  $0.022$  AU), hosted by dwarf K-type stars with effective temperature well below 5000 K ( $T_{\text{eff}} = 4500 \pm 100$ ,  $4595 \pm 45$ ,  $4640 \pm 65$  K respectively). In fact, with the exception of WASP-80 ([Triaud et al. 2015](#)), these are the three coolest TP host stars for which the RM effect has been successfully observed. No additional planet is known to orbit around the three host stars, however for HAT-P-20 a long-term RV linear trend was observed ([Knutson et al. 2014](#); [Deming et al. 2015](#)), possibly caused by a stellar visual companion. Lucky-Imaging observations ([Wöllert & Brandner 2015](#)) put constraints on possible wide companions of WASP-43 and Qatar-2. The high mass of the planets and the small orbital separations also qualify the three systems as interesting candidates to investigate possible stellar activity enhancement induced by the planets.

## 2. Observations and data reduction

### 2.1. Spectroscopic data

All the spectra used in this work were acquired with the HARPS-N spectrograph (wavelength coverage: 383–690 nm, resolving power  $R = 115\,000$ ), installed at the TNG telescope ([Cosentino et al. 2012](#)). The data were reduced by means of the latest version of the HARPS-N Data Reduction Software (DRS; [Cosentino et al. 2014](#); [Smareglia et al. 2014](#)). In addition to 1-D wavelength-calibrated spectra, the DRS provides radial velocities (RVs), calculated by cross-correlating spectra with a numerical mask ([Baranne et al. 1996](#); [Pepe et al. 2002](#); [Lovis & Pepe 2007](#)), and line bisectors. The DRS measures also the Mount Wilson S index and, if the stellar  $B-V$  colour index is lower than 1.2, also the  $\log(R'_{\text{HK}})$  chromospheric activity index is derived ([Lovis et al. 2011](#)).

**WASP-43.** We acquired a time series of 32 spectra, bracketing the transit of WASP-43 b that occurred on the 2013 March 11–12 night. With an exposure time of  $T_{\text{exp}} = 7.5$  min, the spectra have a signal-to-noise ratio (S/N; per pixel in 1-D spectra at 5500 Å) ranging from 12 to 20. Between March 2013 and May 2015, we acquired additional, out-of-transit, spectra at eight different epochs. The RV measurements were obtained using a K5 mask. A log of the transit observations is reported in Table 1 and all the RVs are shown in Table A.1.

**HAT-P-20.** A complete transit of HAT-P-20 b was observed on 2014 March 11–12; the time series of 23 spectra, with exposure times of  $T_{\text{xp}} = 10$  min, started  $\sim 1$  h before ingress and ended  $\sim 1$  h after egress. The S/N (per pixel in 1-D spectra at 5500 Å) degraded from  $\sim 25$  to  $\sim 20$  during the series, with the increase of the air mass. During the observations the target was close

**Table 1.** Log of HARPS-N observations of the planetary transits.

Object	Date <sup>a</sup>	UT start	UT end	$N_{\text{obs}}$	$T_{\text{exp}}$ [s]	Air mass <sup>c</sup>	Moon <sup>b</sup>	2° fiber
WASP-43	2013-03-11	21:46	02:01	32	450	1.59→1.28→1.46	NO	Sky
HAT-P-20	2014-03-11	21:41	01:41	23	600	1.01→1.85	81%/11°	Sky
Qatar-2	2014-04-27	22:08	02:30	17	900	1.51→1.23→1.41	NO	Sky

**Notes.** <sup>(a)</sup> Dates refer to the beginning of the night. <sup>(b)</sup> Fraction of illumination and angular distance from the target. <sup>(c)</sup> Values at first→last exposure, or first→meridian→last exposure.

**Table 2.** Log of photometric observations.

Object	Instr./Tel.	Filter	Date <sup>a</sup>	UT start	UT end	$N_{\text{obs}}$	$T_{\text{exp}}$ [s]	$T_{\text{cad}}$ [s] <sup>d</sup>	Air mass <sup>c</sup>	Moon <sup>b</sup>
WASP-43	AFOSC@1.82 m	R	2011-11-25	02:57	05:27	886	8	10	2.28→1.79	NO
"	CAMELOT@IAC80	R	2013-04-15	21:30	00:44	198	30	56	1.29→1.26→1.84	28%/72°
"	DFOSC@Danish 1.5 m	R	2013-04-19	00:02	01:29	49	100	108	1.10→1.06→1.07	67%/26°
"	CCD Camera@APT2 0.8 m	R	2015-11-12	02:09	04:54	73	120	128	2.92→1.52	NO
HAT-P-20	CAMELOT@IAC80	R	2012-01-16	22:29	01:19	483	15	21	1.19→1.00→1.01	NO
"	CCD Camera@CA 1.23 m	I	2014-10-24	02:02	05:33	109	100	111	1.54→1.02	2%/116°
Qatar-2	CAMELOT@IAC80	R	2014-04-27	22:33	02:51	133	90	116	1.43→1.22→1.49	NO

**Notes.** <sup>(a)</sup> Dates refer to the beginning of the night. <sup>(b)</sup> Fraction of illumination and angular distance from the target. <sup>(c)</sup> Values at first→last exposure, or first→meridian→last exposure. <sup>(d)</sup> Frame acquisition cadence.

(11 deg) to the almost full (81%) Moon, and the Moon RV differed from the star RV by only  $\sim 8 \text{ km s}^{-1}$ , which is  $\sim 1.1$  times the FWHM of the stellar cross-correlation function (CCF). In the CCFs obtained from the sky-illuminated fiber B, the Moon peak is visible and the continuum level is about 2% of the stellar CCF continuum. We corrected for the Moon light contamination by subtracting the fiber B CCF from the fiber A CCF, and then measuring the stellar RV by means of a Gaussian fit to the CCF difference.

Nineteen additional spectra were taken ( $T_{\text{exp}} = 15\text{--}20 \text{ min}$ ,  $S/N \sim 30$ ) in previous and following nights, spanning a time interval of about three years. We estimate that the level of flux contamination in the object fiber from the fainter stellar companion is always well below  $10^{-4}$ . A log of the transit observations is reported in Table 1 and all the RVs are provided in Table A.2.

**Qatar-2.** A time series of 17 spectra was obtained on 2014 April 27–28 covering a full transit of Qatar-2 b. The exposure time was of 15 minutes, resulting in spectra with  $S/N \sim 6$  (per pixel in 1-D spectra at  $5500 \text{ \AA}$ ) and an average RV error of  $\sim 30 \text{ m s}^{-1}$ . A log of the transit observations is reported in Table 1 and the RVs are shown in Table A.3. We note that the in-transit measurements were taken at lower and nearly constant airmass, while the initial and final out-of-transit data points present a relatively wide air-mass excursion.

## 2.2. Photometric data

A total of seven new transit light curves are presented in this study, which were acquired with five different instruments. A log of the photometric observations is reported in Table 2. Below is a description, case-by-case, of the data acquisition processes and the data reduction techniques.

**WASP-43.** A complete transit of WASP-43 b was observed on November 25–26 2011 with the Copernico 1.82 m telescope, at the Asiago Astrophysical Observatory in northern Italy. The

weather conditions were perfect. The 886-frame photometric series, having a constant exposure time of 8 s and a net sampling cadence of about 10 s, was acquired with the Asiago Faint Object Spectrograph and Camera instrument (AFOSC) through a Cousins-*R* filter. The PSF was intentionally defocused to about 8 arcsec FWHM. The images were bias/dark subtracted and flat-field corrected using standard techniques. The transit light curve of WASP-43 b was extracted by STARSKY, an independent, customized software pipeline to perform differential aperture photometry over defocused images (Nascimbeni et al. 2011, 2013). The output light curves from STARSKY are automatically normalized by fitting a linear function to the off-transit continuum.

A second complete transit of WASP-43 b was observed on April 15–16 2013 with the CAMELOT imaging camera (*R* filter) mounted on the IAC80 telescope, at the Teide Astronomical Observatory on the Tenerife island (Spain). The exposure time was set to a constant 30 s, resulting in 198 full-frame images and 56 s of net cadence. The PSF was defocused to about 10 pixel FWHM. The images were corrected for bias and flat-field using standard techniques and then processed by STARSKY to get the final, differential light curve.

Another complete transit of WASP-43 b was observed on April 19–20 2013, using the Danish 1.54 m telescope at ESO La Silla, Chile, the DFOSC imager, and a Cousins *R* filter. The telescope was operated out of focus (see Southworth et al. 2009, for details of the strategy and its application to this telescope and instrument), and the observations were curtailed immediately after egress to capture a time-critical event on another target. The data were reduced using the DEFOT pipeline (Southworth et al. 2014, and references therein), including calibration through master bias and flat-field frames and instrumental flux measurements by aperture photometry. An ensemble comparison star was created from the four good comparison stars in the images, and a linear function of time was applied to rectify the light curve to unit flux outside transit. The weights of the comparison stars, and the coefficients of the linear function, were simultaneously fitted to minimise the scatter in the data outside transit. The resulting light curve has a very low scatter of 0.57 mmag and shows a possible starspot crossing around orbital phase 0.008.



A further complete transit of WASP-43 b was observed with an *R* filter on November 11–12, 2015 within the EXORAP<sup>2</sup> program carried out at the M. G. Fracastoro Station of the INAF-Catania Astrophysical Observatory with a 80 cm f/8 Ritchey-Chretien robotic telescope (APT2), located at Serra la Nave (+14.973° E, +37.692° N, 1725 m a.s.l.) on Mt. Etna, Italy. The telescope is equipped with a set of standard Johnson-Cousins *UBVRI* filters, and an ASPEN camera with a  $2k \times 2k$  e2v CCD 230-42 detector that we operated with a binning factor of 2 (pixel scale 0.94"). Data reduction considered overscan, bias, dark subtraction and flat fielding with the IRAF procedures by using the reduction pipeline specifically developed for the APT2. The night was not photometric and several frames were removed owing to clouds after visual inspection. Fluxes were extracted by aperture photometry as implemented in the IDL routine *aper.pro*. We chose an ensemble of the three least variable stars close to WASP-43 to get its differential photometry. The light curve was normalized to unit flux dividing it by a linear best-fit function of the data outside transit.

**HAT-P-20.** A nearly complete transit of HAT-P-20 b was observed on January 16–17, 2012 with the CAMELOT camera at the IAC80 telescope through an *R* filter. The sky was perfectly clear, but a software problem forced the observer to stop the photometric series just 10 min before the last contact of the transit. The camera was set to read-out only one third of the available frame, to minimize the dead time between exposures. The exposure time was set to a constant 15 s, resulting in 483 images and 21 s of net cadence. The PSF was defocused to about 5 pixel FWHM. The images were corrected for bias and flat-field using standard techniques and then processed by STARSKY to get the final, differential light curve.

A complete transit of HAT-P-20 b was observed on October 24–25, 2014 using the Zeiss 1.23 m telescope at Observatory of Calar Alto, Spain, through a Cousins-*I* filter. The telescope was operated out of focus, and the data were reduced using the DEFOT pipeline. Bias and flat-field calibrations were considered but not used since they had a negligible effect on the results except for a slight increase in shot noise. An ensemble comparison star was made from the four good comparison stars in the images, and a quadratic polynomial versus time was applied to rectify the light curve to unit flux outside transit. The weights of the comparison stars, and the coefficients of the polynomial, were simultaneously fitted to minimise the scatter in the data outside transit.

HAT-P-20 presents a complication because of a nearby star, originally noticed in Bakos et al. (2011). Wöllert & Brandner (2015) found it to lie at a separation of  $6.925 \pm 0.012$  arcsec and be fainter than HAT-P-20 in the Gunn *i* and *z* bands by  $\Delta i = 2.01 \pm 0.08$  and  $\Delta z = 1.67 \pm 0.08$  mag. The point spread function (PSF) of this star partially overlaps that of HAT-P-20. By measuring the PSFs of the two stars, we found that the part of the PSF of the fainter companion within the software aperture for HAT-P-20 produces  $18 \pm 6\%$  of the flux of HAT-P-20 in the passband that we used for the observations. The light curve was renormalized to correct for the contaminating light from the companion.

**Qatar-2.** A transit of Qatar-2 b was observed with the IAC80 telescope at the Teide Observatory on April 27–28, 2014, simultaneously to the spectroscopic observations at the TNG. We acquired a series of 133 slightly defocussed frames with the

CAMELOT camera in the *R*-band. Observations were affected by malfunctioning of the automatic dome tracking, which caused severe vignetting of the images. We corrected the science frames for bias and flat field and then extracted relative photometry of our target. We selected the star and sky apertures as well as the set of comparison stars that minimized the scatter in the data outside transit.

For all the light curves, the timestamps were converted into the BJD(TDB) timescale using subroutines provided by Eastman et al. (2010).

### 3. Stellar parameters

The weighted means of all HARPS-N spectra available for the three targets were used to derive their stellar parameters. In particular, the equivalent widths (EWs) of iron lines taken from the list by Biazzo et al. (2012), together with the *abfind* driver of the MOOG code (Snedden 1973, version 2013), were used to obtain effective temperature ( $T_{\text{eff}}$ ), surface gravity ( $\log g$ ), microturbulence velocity ( $\xi_{\text{mic}}$ ), and iron abundance ( $[\text{Fe}/\text{H}]$ ). This was done by imposing the independence of the iron abundance on the line excitation potentials (for  $T_{\text{eff}}$ ) and EWs (for  $\xi_{\text{mic}}$ ), and the ionization equilibrium between Fe I and Fe II (for  $\log g$ ). The macroturbulence velocity ( $\xi_{\text{mac}}$ ) was fixed to the value obtained using the Valenti & Fischer (2005) relationship depending on  $T_{\text{eff}}$  and  $\log g$ . After fixing the stellar parameters at the values derived through the EWs, a spectral synthesis was performed using the *synth* driver of the same code to measure the projected rotational velocity ( $V \sin I_*$ ) and following the prescriptions given by D'Orazi et al. (2011). All the analysis was performed differentially with respect to the Sun, thanks to a mean Vesta spectrum acquired with HARPS-N.

For further details on the procedures based on EWs and spectral synthesis, we refer to the aforementioned papers, together with other works within the GAPS project (see, e.g., Covino et al. 2013; Damasso et al. 2015a; Malavolta et al. 2016). The results of the spectroscopic analysis applied to determine the stellar parameters are listed in Table 4.

We used the average spectra also to analyse the CaII H&K lines and measure the chromospheric Mount Wilson S-index for WASP-43 and HAT-P-20, while for Qatar-2 the S/N was too low to derive a reliable measurement. We then calculated the  $\log(R'_{\text{HK}})$  index, following the prescriptions in Suárez Mascareño et al. (2015)<sup>3</sup>. We used our determinations of the  $T_{\text{eff}}$  and the empirical calibrations reported in Flower (1996) to derive the required intrinsic *B*–*V* colour index. We obtain  $B-V = 1.19 \pm 0.06$  and  $1.135 \pm 0.025$  for WASP-43 and HAT-P-20, respectively. We notice that the observed *B*–*V* colors (see Table 4) are slightly larger than the intrinsic ones, which is possibly due to interstellar reddening. The values of the *S* and  $\log(R'_{\text{HK}})$  indices are reported in Table 4.

### 4. Light curves and radial velocities analysis

We developed a code within the MATLAB software ambient<sup>4</sup> for modelling and fitting planet transits observations. The code can

<sup>3</sup> We did not use the HARPS-N DRS for the measurement of the *S*-index because its application to average spectra is not straightforward. Also, since the *B*–*V* colors of our targets are close to 1.2, for the calculation of the  $\log(R'_{\text{HK}})$  index, we preferred to follow Suárez Mascareño et al. (2015) rather than Lovis et al. (2011).

<sup>4</sup> MATLAB R2015b, Optimization Toolbox 7.3 and Curve Fitting Toolbox 3.5.2, The MathWorks, Inc., Natick, Massachusetts, United States.

<sup>2</sup> EXOplanetary systems Robotic APT2 Photometry

**Table 3.** Results of the individual analyses of the four WASP-43 b and two HAT-P-20 b transit light curves.

Instr./Tel.	$a/R_\star$	$R_p/R_\star$	$i_p [^\circ]$	$T_{14}$ [day]	$T_C$ [BJD-2 400 000]	$u$
WASP-43						
AFOSC@1.82 m	$4.896 \pm 0.084$	$0.1590 \pm 0.0017$	$82.27 \pm 0.29$	$0.0512 \pm 0.0010$	$55\,891.67847 \pm 0.00018$	$0.66 \pm 0.13$
CAMELOT@IAC80	$4.989 \pm 0.070$	$0.1594 \pm 0.0016$	$82.12 \pm 0.21$	$0.04943 \pm 0.00073$	$56\,398.47228 \pm 0.00016$	$0.511 \pm 0.075$
DFOSC@Danish 1.5 m	$5.039 \pm 0.052$	$0.15538 \pm 0.00086$	$82.03 \pm 0.19$	$0.04792 \pm 0.00036$	$56\,402.539119 \pm 0.000088$	$0.484 \pm 0.057$
CCD Camera@APT2 0.8 m	$4.737 \pm 0.090$	$0.1702 \pm 0.0021$	$81.36 \pm 0.48$	$0.05156 \pm 0.00030$	$57\,339.66239 \pm 0.00011$	$0.54 \pm 0.11$
HAT-P-20						
CAMELOT@IAC80	$10.74 \pm 0.44$	$0.1534 \pm 0.0034$	$86.32 \pm 0.40$	$0.0796 \pm 0.0016$	$55\,943.52369 \pm 0.00025$	$0.51 \pm 0.12$
CCD Camera@CA 1.23 m	$11.48 \pm 0.33$	$0.1542 \pm 0.0027$	$87.00 \pm 0.26$	$0.0791 \pm 0.00048$	$56\,955.634275 \pm 0.000055$	$0.675 \pm 0.068$

**Notes.** The columns report the following parameters:  $a/R_\star$  is the ratio between the semi-major orbital axis and the stellar radius;  $R_p/R_\star$  is the planet to star radii ratio;  $i [^\circ]$  is the orbital inclination angle;  $b$  is the transit impact parameter;  $T_{14}$  is the transit duration;  $T_C$  is the epoch of mid-transit;  $u$  is the coefficient of the linear limb-darkening law according to Eq. (1) in [Claret & Bloemen \(2011\)](#).

simultaneously fit any number of (in- and out-transit) RV data sets, as well as transit light curves in different filters.

The model considers the parameters necessary to fully describe the planet and star position and velocity vectors at any given time, i.e., the masses of the star  $M_\star$  and of the planet  $M_p$ , the orbital period  $P$  and eccentricity  $e$ , the epoch  $\tau$  and argument  $\omega$  of periastron, the systemic RV  $\gamma$ ; the orbital space orientation is described by the inclination angle  $i_p$  and the misalignment angle  $\lambda$ . The third angle, the longitude of the ascending node, is not considered since it does not affect the RV and photometric measurements. Other parameters necessary to model the RM effect and the light curves are the radii of the star  $R_\star$  and of the planet  $R_p$ , the stellar projected rotational velocity  $V \sin I_\star$ , and the limb-darkening coefficients. Our model implements each of the five equations (linear, quadratic, root-square, logarithmic, and a 4-coefficient law) proposed by [Claret & Bloemen \(2011\)](#) to describe the limb-darkening law. Other effects that can affect the measurements, such as stellar surface inhomogeneities (spots, faculae, etc.), stellar differential rotation and convective blue-shift, are not included in the model.

For the analysis of the RM effect, we implemented a numerical model based on the following assumptions. We tried to reproduce the observed CCF by modelling an average photospheric line profile. The stellar disc is sampled by a matrix of  $1000 \times 1000$  elements, each element being represented by a Gaussian line profile with a given width  $\sigma_{el}$ , Doppler-shifted according to the stellar rotation, and weighted by appropriate limb-darkening coefficients.  $\sigma_{el}$  is also a parameter of the fit, however we always fix it, since it turned out that the model RVs are largely insensitive to its exact value. The value of  $\sigma_{el}$  is chosen by adding in quadrature the values of  $\xi_{mic}$  and  $\xi_{mac}$ . The resulting line profile is then convolved by the instrumental profile of HARPS-N, assumed Gaussian with  $\sigma_{IP} = 1.108 \text{ km s}^{-1}$ . The model also takes into account the actual area of the stellar photospheric disc occulted and the smearing owing to the planet's displacement during an exposure. The corresponding RV shift is then computed by a Gaussian fit of the resulting line profile, analogously to the HARPS-N DRS. The same numerical approach is also used for the modelling and analysis of the light curves. Limb darkening coefficients can be fitted independently for each light curve.

The best-fitting model to the data is found via a sigma-weighted, robust least-squares minimization. The region of the parameters space to be explored can be restricted by setting upper and lower limits to the parameter values. Most importantly, any number of linear and non-linear constraints can be set: this enables us to place limits on other parameters (such as  $K$ ,  $T_{14}$ ,  $b$ ,

etc.), even though they are not direct parameters of the fit. The mass of the star is preliminarily determined from evolutionary track models, adopting the values of the atmospheric parameters that were determined previously and using the  $a/R_\star$  value derived from an independent fit of the light curve. The uncertainties on the best-fit values are obtained by means of a bootstrap algorithm.

We use our code to analyse all the RVs and light curves presented in this work. Depending on the type and quality of our data as compared to those in literature, we decide whether a parameter is to be fitted or fixed to the value available in the literature.

#### 4.1. WASP-43

To begin with, we analysed the four transit light curves (LCs) taken individually. The best-fit values of the relevant parameters are reported in Table 3. Following [Sozzetti et al. \(2007\)](#), we used the  $a/R_\star$  values to derive the stellar density, resulting in a sigma-clipped weighted average of  $\rho_\star = 2.47 \pm 0.11 \rho_\odot$ . The sigma-clipping effectively excluded the APT2 value that is off by  $>2\sigma$  with respect to the other three. The stellar density, together with our determinations of  $T_{eff}$  and  $[\text{Fe}/\text{H}]$ , was used to estimate the mass of the star by comparison with the Yonsei-Yale evolutionary tracks ([Demarque et al. 2004](#)). Following [Southworth \(2011\)](#), we accounted for systematic uncertainties in the stellar models by adding an extra 5% to the formal errors, and obtained  $M_\star = 0.688 \pm 0.037 M_\odot$ .

Our determinations of the four epochs of mid-transit are compatible with the most recently published ephemerides ([Hoyer et al. 2016](#); [Jiang et al. 2016](#); [Ricci et al. 2015](#); [Chen et al. 2014](#)). In the following analyses, we fixed the orbital period to the value reported in [Hoyer et al. \(2016\)](#), where all the LCs available in literature were analysed homogeneously:  $P = 0.813473978 \pm 3.5 \times 10^{-8}$  days.

We then analysed the out-of-transit RVs. In addition to our 22 measurements, we also considered the 23 CORALIE RV values reported in [Hellier et al. \(2011\)](#) and [Gillon et al. \(2012\)](#), allowing for a constant RV offset between the two data sets. We found that the best-fit circular and eccentric orbits were virtually indistinguishable from each other, therefore we opted for fixing  $e = 0$ . Strong constraints on the eccentricity were already put by [Gillon et al. \(2012;  \$0.0035^{+0.0060}\_{-0.0025}\$ \)](#) and [Blecic et al. \(2014;  \$0.010^{+0.010}\_{-0.007}\$ \)](#), based also on the timing of secondary eclipse. From the best-fit value of the RV curve semi-amplitude  $K = 551 \pm 8 \text{ m s}^{-1}$ , and the orbital inclination angle that we derived from the LCs analysis (see Table 3), we calculated the planetary mass.

**Table 4.** Planetary and stellar parameters for the three systems here studied.

Parameter [unit]	WASP-43	HAT-P-20	Qatar-2
$B$ [mag] <sup>j</sup>	13.796 ± 0.022	12.539 ± 0.075	14.582 ± 0.022
$V$ [mag] <sup>j</sup>	12.464 ± 0.028	11.339 ± 0.031	13.417 ± 0.023
$J$ [mag] <sup>k</sup>	9.995 ± 0.024	9.276 ± 0.022	11.350 ± 0.026
$H$ [mag] <sup>k</sup>	9.397 ± 0.025	8.743 ± 0.021	10.794 ± 0.022
$K$ [mag] <sup>k</sup>	9.267 ± 0.026	8.601 ± 0.019	10.619 ± 0.021
Space velocity ( $U, V, W$ ) [km s <sup>-1</sup> ]	(-2.7, -10.8, -20.4)	(19.1, -27.7, -2-1.4)	–
<i>Stellar spectra characterization</i>			
Effective temperature, $T_{\text{eff}}$ [K]	4500 ± 100	4595 ± 45	4640 ± 65
Surface gravity, $\log g_{\star}$ [cm s <sup>-2</sup> ]	4.50 ± 0.20	4.52 ± 0.09	4.51 ± 0.12
Iron abundance, [Fe/H]	-0.01 ± 0.15	0.22 ± 0.09	0.13 ± 0.10
Microturbulence vel., $\xi_{\text{mic}}$ [km s <sup>-1</sup> ]	1.00 ± 0.15	0.74 ± 0.27	0.90 ± 0.35
Macroturbulence vel., $\xi_{\text{mac}}$ [km s <sup>-1</sup> ] <sup>l</sup>	2.03	2.17	2.24
Proj. rot. vel., $V \sin I_{\star}$ [km s <sup>-1</sup> ]	2.6 ± 0.5	2.0 ± 0.5	2.0 ± 1.0
$\langle \text{MW S-index} \rangle$	1.647 ± 0.059	1.20 ± 0.13	–
$\langle \log(R'_{\text{HK}}) \rangle$	-4.35 ± 0.10	-4.40 ± 0.06	–
<i>RV and photometric data fit</i>			
Star mass, $M_{\star}$ [ $M_{\odot}$ ]	0.688 ± 0.037	0.742 ± 0.042	0.798 ± 0.040
Planet mass, $M_{\text{p}}$ [ $M_{\text{J}}$ ]	1.998 ± 0.079	7.22 ± 0.36	2.616 ± 0.071
Star radius, $R_{\star}$ [ $R_{\odot}$ ]	0.6506 ± 0.0054	0.6796 ± 0.0054	0.793 ± 0.024
Planet radius, $R_{\text{p}}$ [ $R_{\text{J}}$ ]	1.006 ± 0.017	1.025 ± 0.053	1.281 ± 0.039
Orbital period, $P$ [day]	0.813473978 ± 0.000000035 <sup>a</sup>	2.875316938 ± 0.000000019	1.33711647 ± 0.000000026 <sup>f</sup>
Eccentricity, $e$	0 (fixed)	0.0172 ± 0.0016	0 (fixed)
Longitude of periastron, $\omega$ [deg]	90 (fixed)	342.7 ± 7.3	90 (fixed)
Orbital inclination, $i_{\text{p}}$ [deg]	82.109 ± 0.088	86.88 ± 0.31	86.12 ± 0.08 <sup>f</sup>
Epoch of periastron, $\tau$ [BJD]	–	2455942.681 ± 0.016	–
Barycentric RV, $\gamma$ [m s <sup>-1</sup> ]	-3595.5 ± 4.3 <sup>b</sup>	-18087.44 ± 0.7 <sup>g</sup>	-23977.5 ± 7.1
Barycentric RV, $\gamma_2$ [m s <sup>-1</sup> ]	-3588.1 ± 2.7 <sup>c</sup>	-18093.36 ± 0.8 <sup>g</sup>	–
Proj. spin-orbit angle, $\lambda$ [deg]	3.5 ± 6.8	-8.0 ± 6.9	15 ± 20
Proj. rot. vel., $V \sin I_{\star}$ [km s <sup>-1</sup> ]	2.26 ± 0.54	1.85 ± 0.27	2.09 ± 0.58
Stellar rotational period, $P_{\text{rot}}$ [day]	15.6 ± 0.4 <sup>d</sup>	14.48 ± 0.02 <sup>e</sup>	18.77 ± 0.29
<i>Derived parameters</i>			
Orbital semi-major axis, $a$ [AU]	0.01504 ± 0.00029	0.03593 ± 0.00029	0.02205 ± 0.00037
Transit duration, $T_{14}$ [day]	0.0485 ± 0.010	0.07900 ± 0.00052	–
Impact parameter, $b$	0.689 ± 0.013	0.622 ± 0.059	0.405 ± 0.028
$a/R_{\star}$	4.97 ± 0.14	11.36 ± 0.25	5.98 ± 0.28
$R_{\text{p}}/R_{\star}$	0.1588 ± 0.0040	0.155 ± 0.010	0.166 ± 0.010
Spin-orbit angle $\Psi$ [deg]	<20 <sup>i</sup>	36 <sup>+10</sup> <sub>-12</sub>	<43 <sup>i</sup>
Star incl. angle $I_{\star}$ [deg]	>72 <sup>i</sup>	53 ± 12	>58 <sup>i</sup>
RV-curve semi-amplitude, $K$ [m s <sup>-1</sup> ]	551.0 ± 3.2	1249.5 ± 1.2	558.7 ± 5.9 <sup>h</sup>
Star density, $\rho_{\star}$ [g cm <sup>-3</sup> ]	2.526 ± 0.080	2.36 ± 0.16	2.240 ± 0.023 <sup>f</sup>
Star surface gravity, $\log g_{\star}$ [cm s <sup>-2</sup> ]	4.647 ± 0.011	4.643 ± 0.020	4.541 ± 0.048
Planet density, $\rho_{\text{p}}$ [g cm <sup>-3</sup> ]	2.43 ± 0.14	8.31 ± 0.38	1.54 ± 0.20
Planet surface gravity, $\log g_{\text{p}}$ [cm s <sup>-2</sup> ]	3.696 ± 0.018	4.231 ± 0.019	3.597 ± 0.038
Planet equilibrium temperature, $T_{\text{p}}$ [K]	1426.7 ± 8.5	964 ± 10	1342 ± 15

**Notes.** <sup>(a)</sup> Adopted from Hoyer et al. (2016); <sup>(b)</sup> CORALIE data; <sup>(c)</sup> HARPS-N data; <sup>(d)</sup> adopted from Hellier et al. (2011); <sup>(e)</sup> value adopted from Granata et al. (2014), error derived by us with an independent re-analysis of the data; <sup>(f)</sup> adopted from Mancini et al. (2014); <sup>(g)</sup> off-transit ( $\gamma$ ) and in-transit ( $\gamma_2$ ) HARPS-N data; <sup>(h)</sup> adopted from Bryan et al. (2012); <sup>(i)</sup> at the 68% level of confidence. <sup>(j)</sup> APASS catalogue (Henden et al. 2016); <sup>(k)</sup> 2MASS catalogue (Cutri et al. 2003) <sup>(l)</sup> fixed to the values obtained following Valenti & Fischer (2005).

The next step was to analyse the RV time-series covering the planetary transit and to measure the RM effect. By fixing the other relevant parameters, as obtained by the LCs and out-of-transit RVs fits, we derived a best-fit value for the sky-projected spin-orbit angle  $\lambda$  and stellar rotational velocity  $V \sin I_{\star}$ .

Finally, using the values obtained from the previous analyses as a first guess, we made a global joint fit of all the RVs and LCs to derive a fully consistent set of best-fit orbital and physical parameters. The final results are reported in Table 4. Aside from our new determination of  $\lambda = 3.5 \pm 6.8$  deg, the values of the stellar and planet parameters are consistent with previous

measurements (Hellier et al. 2011; Gillon et al. 2012; Chen et al. 2014). The four phase-folded LCs and their best-fit models are displayed in Fig. 1. The RV measurements with the orbital and RM best-fit curves are shown in Fig. 2.

By combining our measurements of  $R_{\star}$  and  $V \sin I_{\star}$  with the stellar rotational period  $P_{\text{rot}} = 15.6 \pm 0.4$  days reported in Hellier et al. (2011), we can estimate (see formula (8) in Winn et al. 2007) the value of  $\sin I_{\star}$  to be  $1.08 \pm 0.25$ . With  $\sin I_{\star} > 1$  being physically impossible, we deduce that the true value of  $\sin I_{\star}$  must be very close to 1, hence  $I_{\star} \approx 90$  deg. In fact we derive that  $I_{\star} > 72$  deg with a 68% level of confidence.

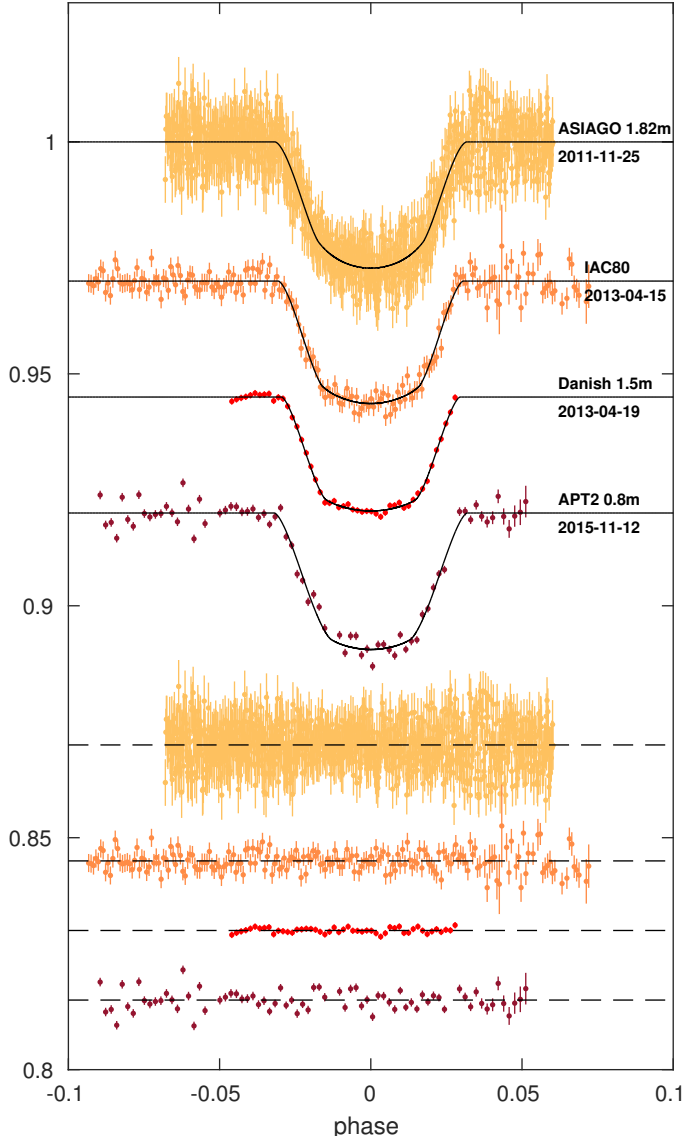


**Fig. 1.** WASP-43 normalized light curves with best-fit models superimposed. For clarity a vertical offset was applied to the different LCs. The lower part of the diagram shows the best-fit residuals. Data are phase-folded according to the orbital period reported in Table 4 and the epochs of mid-transit reported in Table 3. For each LC we report the telescope and the date of observation. In all cases a Johnson *R* filter was used.

Similarly (see formula (7) in Winn et al. 2007), we derive that the true orbital misalignment angle  $\Psi$  is  $<20$  deg with a 68% level of confidence.

#### 4.2. HAT-P-20

HAT-P-20 shows clear signatures of a high level of stellar activity. Granata et al. (2014) analysed the SuperWASP photometry of HAT-P-20 to derive the rotational period and found a modulation with a peak-to-valley amplitude as high as  $\sim 0.04$  mag. Both our two transit light curves show evidence of the planet crossing a star spot (see Fig. 3). Also, the analysis of the RV measurements reveals jitter at the level of  $\sim 20$  m s $^{-1}$ .

We first analysed the two LCs individually. In Table 3, we report the values of the fitted transit parameters. We find values for  $R_p/R_\star$  that are consistent with each other but significantly larger than any of the values reported in Granata et al. (2014).

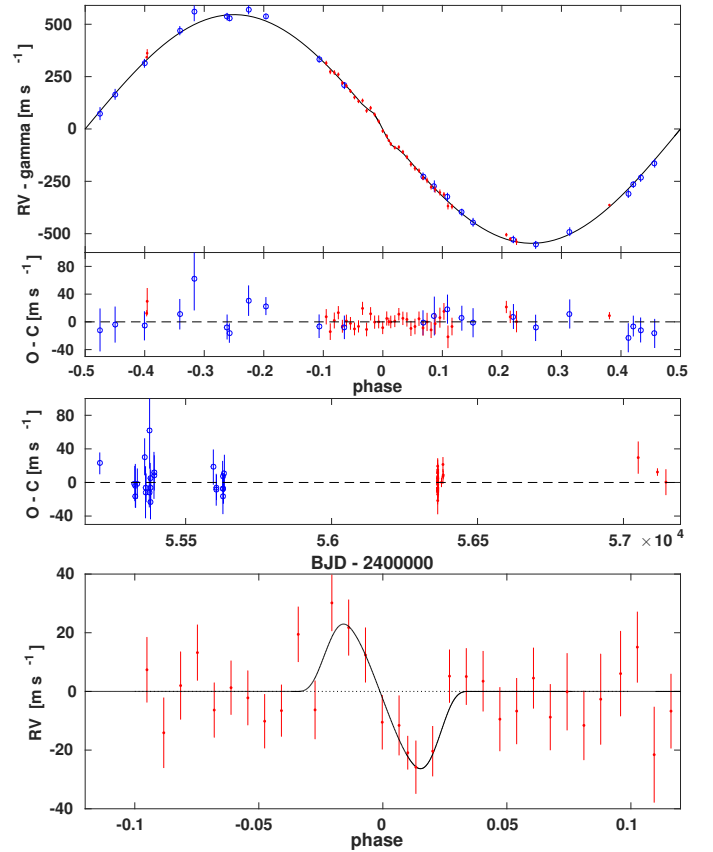


**Fig. 2.** WASP-43 radial velocities. Red dots represent HARPS-N data while blue open circles are CORALIE data. *Top panels:* phase-folded RVs with the best-fit RV curve superimposed, and below the corresponding residuals. *Middle panel:* RV residuals plotted as a function of the Barycentric Julian Date (BJD) show no evidence of a long term RV trend. *Bottom panel:* zoom in the RV time-series covering the transit. To highlight the RM effect, the orbital RV trend was subtracted.

A possible explanation for this discrepancy is that the two transits observed by us occurred during a phase of higher stellar spots filling factor (Ballerini et al. 2012). The two light curves with the best-fit transit model superimposed are displayed in Fig. 3. Thanks to the robust algorithm the best-fit is only marginally affected by the spot crossing regions.

By adding our two determinations of the epoch of mid-transit to the values listed in Granata et al. (2014), we calculated new transit ephemerides. A weighted least-square linear fit (see Fig. 4) yielded:

$$T_0 (\text{BJD}_{\text{TDB}}) = (2455\,598.484742 \pm 0.000073) + N(2.87531694 \pm 0.00000019). \quad (1)$$

Fixing the values obtained for  $T_0$  and  $P$ , we then performed a global fit of the two light curves and all the HARPS-N RVs. We treated the RV time-series on the night of the transit as an independent data-set by adding a parameter to the fit that represents the barycentric radial velocity for the night of the transit. This was necessary to account for an RV offset most likely caused by the stellar jitters.

The phase-folded RVs and the best-fit model are displayed in the top panel of Fig. 5. Our data confirm that HAT-P-20b moves on an orbit with a small but significant eccentricity. Our best-fit value is  $e = 0.0172 \pm 0.0016$ , in agreement with previously reported values ( $e = 0.015 \pm 0.005$ , Bakos et al. 2011;  $e = 0.0158^{+0.0041}_{-0.0036}$ , Knutson et al. 2014;  $e = 0.0171^{+0.0018}_{-0.0016}$ ,



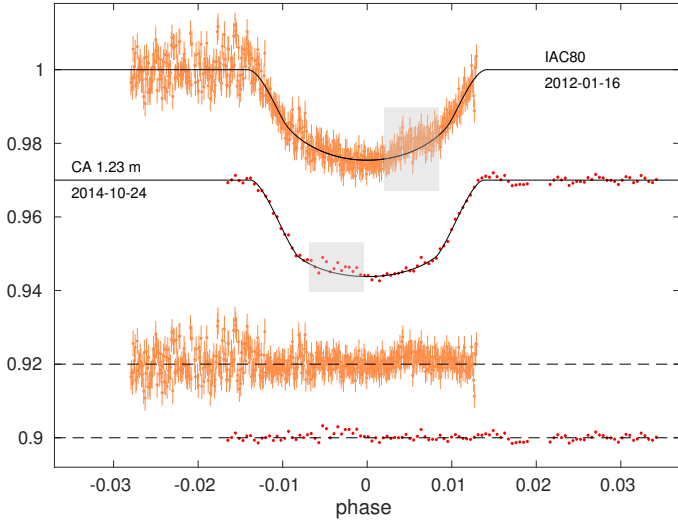


**Fig. 3.** HAT-P-20 light curves (*top*) and best-fit residuals (*bottom*). Data are phase-folded according to the best-fit period reported in Eq. (1). For each LC the telescope and date of observation are indicated. For the IAC80 LC, a Johnson-*R* filter was used. For the CA LC, a Cousins-*I* filter. Shaded areas indicate phases of possible spot crossing.

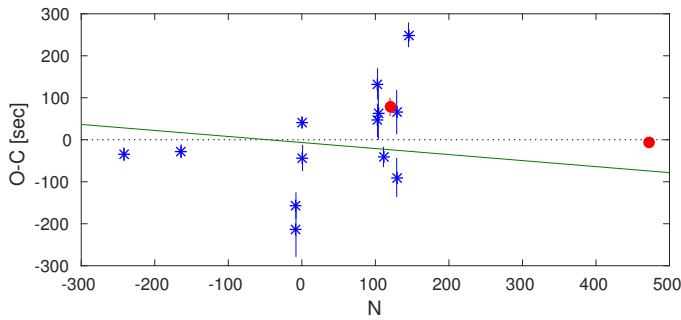


**Fig. 4.** O-C diagram obtained by a linear fitting (i.e., constant period) of the HAT-P-20 b mid-transit epochs. Blue asterisks are from Granata et al. (2014), red dots correspond to the two transit observations reported in this work. The green continuous line represents the ephemerides calculated in Granata et al. (2014).

Deming et al. 2015). For the mass of the planet we find  $M_p = 7.22 \pm 0.36 M_J$ , in agreement with the literature value ( $M_p = 7.24 \pm 0.18 M_J$ , Knutson et al. 2014). However, given the larger planet radius ( $R_p = 1.025 \pm 0.053 R_J$ ) that we obtain from the transit light curves analysis, we derive a planet density that is significantly lower ( $\rho_p = 8.31 \pm 0.38 \text{ g cm}^{-3}$ ) than previously reported ( $13.78 \pm 1.50 \text{ g cm}^{-3}$ , Bakos et al. 2011). After subtraction of the best-fit 1-planet model, the RV residuals show a scatter ( $\text{rms} \approx 16 \text{ m s}^{-1}$ ) that largely exceeds the typical internal RV uncertainties ( $\sigma \approx 3.5 \text{ m s}^{-1}$ ) (see mid-panel in Fig. 5). A frequency analysis of the RV residuals does not reveal any significant periodicity, therefore we ascribe the large residuals to stellar activity-induced RV jitter. However, we have checked that there is no evident correlation between the RV residuals and the CCF bisector span. In the computation of the errors on the best-fit parameters, we accounted for a RV-jitter term. Knutson et al. (2014), with 13 RV measurements spanning 1331 days, report a negative linear trend of  $-0.0141^{+0.0073}_{-0.0078} \text{ m s}^{-1} \text{ day}^{-1}$ . By allowing for a linear trend in our fit of HARPS-N RVs (19 out-of-transit data points spanning 137 days), we obtain a positive, but not significant, trend of  $7.5\text{e-}03 \pm 15\text{e-}03 \text{ m s}^{-1} \text{ day}^{-1}$ .

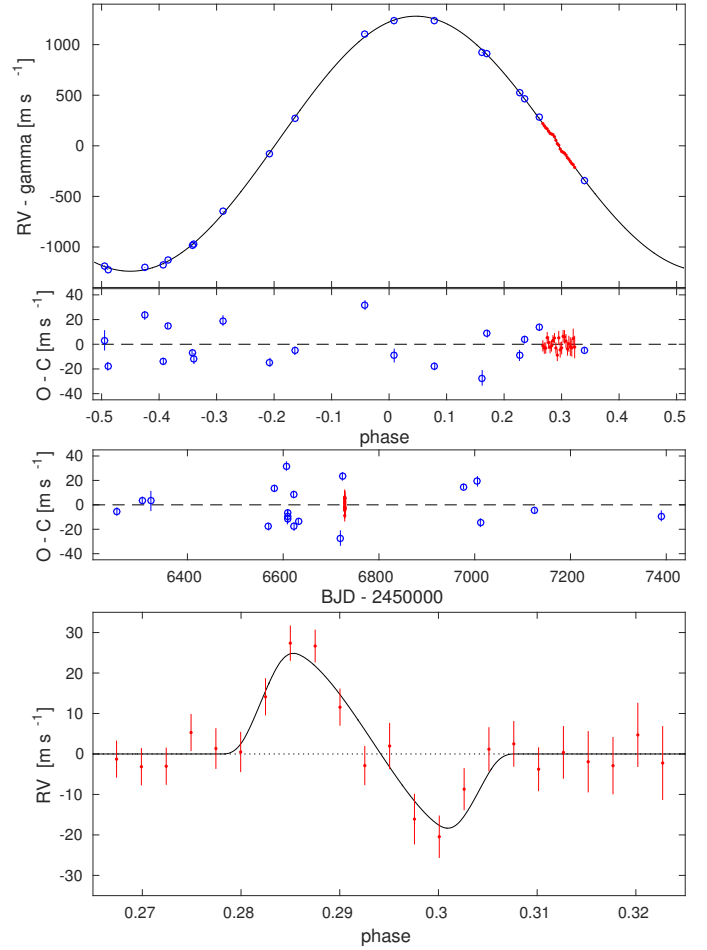


**Fig. 5.** HAT-P-20 radial velocities. Data taken during the night of the transit are displayed with red dots. *Top panels:* phase-folded RVs with the best-fit RV curve superimposed, and below the corresponding residuals. *Middle panel:* RV residuals plotted as a function of the Barycentric Julian Date (BJD) show no evidence of a long term RV trend. *Bottom panel:* RV time-series covering the transit. To highlight the RM effect, the orbital RV trend was subtracted.

The best fit model of the RM effect gives  $V \sin I_\star = 1.85 \pm 0.27 \text{ km s}^{-1}$ , slightly lower but consistent with the spectral synthesis determination, and  $\lambda = -8.0 \pm 6.9 \text{ deg}$  which is marginally different from zero. Using the value of the stellar rotational period  $P_{\text{rot}} = 14.48 \pm 0.02 \text{ days}$  reported in Granata et al. (2014), we estimate the stellar spin-axis inclination to be  $I_\star = 53 \pm 12 \text{ deg}$ , and the true planet orbital misalignment angle  $\Psi = 36^{+10}_{-12} \text{ deg}$ , meaning that HAT-P-20 b lies on a significantly inclined orbit. As a note of caution on this result, we emphasise that, if the star experiences a significant differential rotation, we underestimate  $V \sin I_\star$ , while higher values of  $V \sin I_\star$  translate to  $I_\star$  closer to  $90 \text{ deg}$  and  $\Psi$  closer to  $0 \text{ deg}$ .

#### 4.3. Qatar-2

The Qatar-2 b transit photometry, which we acquired simultaneously to the HARPS-N RV monitoring, is affected by a trend that starts shortly after the mid-transit phase and extends well beyond the end of the transit (see the top panel in Fig. 6). We traced back the origin of this trend to image vignetting (see Sect. 2.2), but we could not reliably model and correct for it. Therefore, although we show the light curve, it was not actually used in our data fit. Instead, we adopted the relevant parameters

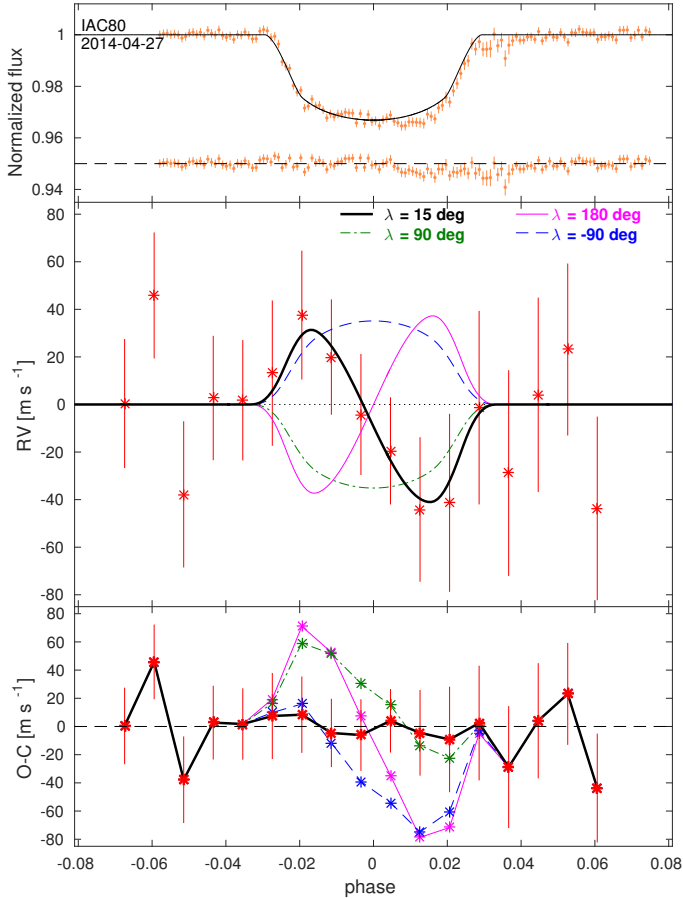


**Fig. 6.** Simultaneous photometric and RV monitoring of the transit of Qatar-2b. *Top panel:* IAC80 photometric data. The black line is the model light curve, but it is not a fit to the data (see text in Sect. 4.3 for details). *Middle panel:* RV time-series covering the transit (red asterisks). To highlight the RM effect, the orbital RV trend was subtracted. Together with our best-fit model (black thick line), we also show models with  $V \sin I_\star = 2.0 \text{ km s}^{-1}$  and  $\lambda = -90, 90, 180 \text{ deg}$  (dashed blue, dot-dashed green, magenta lines, respectively). *Bottom panel:* RV residuals for the best-fit model of the RM effect and for the other three models shown in the *middle panel*.

from Mancini et al. (2014), who analysed a series of high quality transit light curves of Qatar-2b (see Table 4). Specifically, we used the stellar density  $\rho_\star = 2.240 \pm 0.023 \text{ g cm}^{-3}$  from Mancini et al. (2014), together with our spectroscopic determinations of  $T_{\text{eff}}$  and  $[\text{Fe}/\text{H}]$ , as input to the Yonsei-Yale evolutionary tracks to estimate the stellar mass  $M_\star = 0.798 \pm 0.040 M_\odot$  and radius  $R_\star = 0.793 \pm 0.024 R_\odot$ . Then, we consistently scaled the values of the planet mass  $M_p = 2.616 \pm 0.071 M_J$  and radius  $R_p = 1.281 \pm 0.039 R_J$ . As a check, we verified that the light curve model, calculated adopting those parameters, adjusts well to the first half of our IAC80 photometric data (see top panel in Fig. 6).

The RV time-series covering the Qatar-2b transit was fitted with the RM model, setting free only three parameters:  $\lambda$ ,  $V \sin I_\star$  and  $\gamma$ . The best-fit values are reported in Table 4 and the RV measurements with the best-fit solution are displayed in the middle panel of Fig. 6. With only eight in-transit data points and relatively large RV errors, in comparison with the amplitude of the RM effect, our detection may not appear statistically significant. However, we note that the best-fit value of  $V \sin I_\star = 2.09 \pm 0.58 \text{ km s}^{-1}$  agrees with the value of

$2.0 \pm 1.0 \text{ km s}^{-1}$  derived from our spectroscopic analysis. To assess the reliability of our estimate of  $\lambda = 15 \pm 20 \text{ deg}$ , we then computed RM models with  $V \sin I_\star$  fixed to  $2.0 \text{ km s}^{-1}$  for three different values of  $\lambda$  (90, 180,  $-90 \text{ deg}$ ), shown in Fig. 6. By comparing the different models, it appears that the data enable us to discriminate between different values of  $\lambda$ . Furthermore, we note that the best-fit value of  $\lambda$  we obtain is consistent with a previous determination of  $\lambda = 4.3 \pm 4.5 \text{ deg}$ , as obtained by Mancini et al. (2014) using the spot-crossing method.

#### 4.3.1. Stellar rotational period

We retrieved the publicly available QES (Qatar Exoplanet Survey) photometric monitoring data of Qatar-2 (Bryan et al. 2012). The time series consists of 1217 data points distributed over 54 nights and spanning an interval of 84 days. After removing some evident outliers (44 points), we analysed the remaining points for possible periodic signals, both before and after removing the in-transit data ( $-0.04 < \text{phase} < 0.04$ ; 94 points). The Lomb-Scargle periodograms (top panel in Fig. 7) show two peaks which become prominent after discarding the in-transit points, corresponding to periods  $P_1 \sim 18.7 \text{ days}$  and  $P_2 \sim P_1/2$ . To assess the significance of these peaks, we computed the periodograms for  $10^5$  mock data sets, obtained by randomly permuting the time-stamps of the original data set. Then, we calculated false alarm probability (FAP) levels; for instance, a 1% FAP level means that in  $10^3$  out of  $10^5$  cases a peak higher than that level was found in the periodograms, over the entire frequency range  $[10^{-3}, 1.02] \text{ days}^{-1}$ . In this way, we estimate the FAP associated with the peak at  $P_1$  to be 0.9%. In the bottom panel of Fig. 7 we show the Qatar-2 QES photometry, binned on a night-by-night basis, phase-folded with the period  $P_1$ , and an arbitrarily chosen reference epoch. We consider  $P_1$  as the stellar rotational period. The light curve shows a clear minimum around phase 0.5 and then a rather flat maximum from 0.8 to 0.3. The strong harmonic at  $P_1/2$  observed in the periodogram also points to an asymmetric light curve. This shape can be explained by a single cold spotted region visible for half period only, perfectly compatible with the equator-on orientation of our line of sight. We used a bootstrap method, applied to the binned data, to derive the uncertainty on the period, obtaining  $P_{\text{rot}} = 18.77 \pm 0.29 \text{ days}$ . Very recently two independent works (Močnik et al. 2016; Dai et al. 2017) reported on the analysis of K2 photometric time-series for Qatar-2, and both determined a stellar rotational period in agreement with our result, and confirmed that the planet is aligned.

Using the values of  $P_{\text{rot}}$ ,  $V \sin I_\star$ , and  $R_\star$ , we derive that  $I_\star > 58 \text{ deg}$  with a 68% confidence level. From our determination of  $\lambda = 15 \pm 20 \text{ deg}$ , we estimate that the true spin-orbit angle is  $\Psi < 43 \text{ deg}$  with a 68% confidence level.

## 5. Discussion

### 5.1. Stellar activity

It has been speculated that the presence of close-in giant planets could cause an enhancement of the activity level of their host stars, via star-planet tidal interactions and/or magnetic coupling (Cuntz et al. 2000; Lanza 2008, 2012). Many observational studies have looked for correlations between stellar activity indicators and the presence and properties of exoplanets (e.g. Maggio et al. 2015; Borsa et al. 2015). Shkolnik (2013), taking into consideration the 272 known FGK planetary hosts observed by GALEX, only find tentative evidence that hot-Jupiters host stars are more FUV-active; Poppenhaeger et al. (2010),

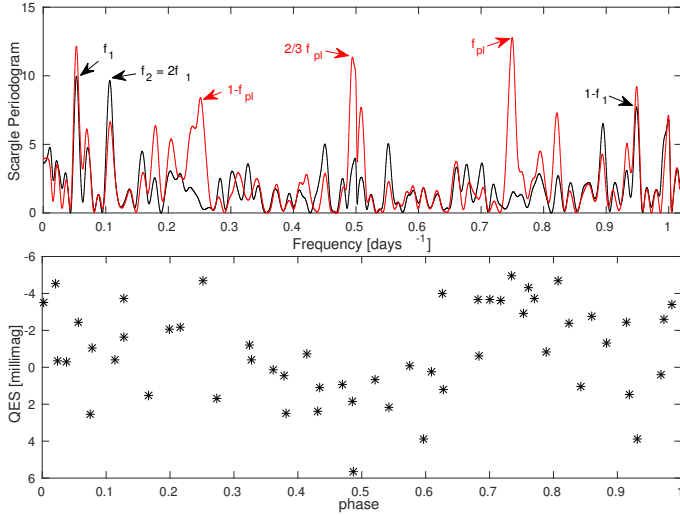


**Fig. 7.** *Top panel:* Scargle periodogram of the QES photometric monitoring data of Qatar-2, before (red line) and after (black line) removing the in-transit points.  $f_{\text{pl}}$  corresponds to the planet orbital period; we deem the peak at  $f_1$  to originate from a photometric modulation at the stellar rotational period. *Bottom panel:* nightly averaged photometric data phase-folded at the  $P_1 \equiv 1/f_1 = 18.77$  days period.

analyzing planet-bearing stars within 30 pc, conclude that there are no correlations of X-ray luminosity or the activity indicators  $L_X/L_{\text{bol}}$  with planetary parameters. Krejčová & Budaj (2012) find statistically significant evidence that the equivalent width of the Ca II K line emission and  $\log(R'_{\text{HK}})$  activity parameter of the host star vary with the mass and orbital semi-major axis of the planet. In a similar study, which considered, however, a sample of planets at larger orbital separations, Canto Martins et al. (2011) do not find significant correlations.

We have found that HAT-P-20 and WASP-43 have values of  $\log(R'_{\text{HK}})$  (see Table 4) that place them among the most active planet-host stars, reinforcing the Krejčová & Budaj (2012) results (see in particular their Figs. 3 and 5). Suárez Mascareño et al. (2015), by studying a sample of stars monitored with the HARPS spectrograph for which the presence of hot-Jupiters can be excluded with high confidence, find an empirical tight correlation between the stellar rotational period  $P_{\text{rot}}$  and the average  $\log(R'_{\text{HK}})$  (see also Noyes et al. 1984 and Mamajek & Hillenbrand 2008). According to their Eq. (9), based on the measured  $P_{\text{rot}}$ , WASP-43 and HAT-P-20 should have a  $\log(R'_{\text{HK}})$  of  $-4.62 \pm 0.07$  and  $-4.57 \pm 0.07$  respectively, lower than the measured values by  $0.27 \pm 0.12$  and  $0.17 \pm 0.08$  respectively. Thus, we have found that, at the  $2\text{-}\sigma$  level of confidence, both WASP-43 and HAT-P-20 show an enhanced level of chromospheric activity as measured by the  $\log(R'_{\text{HK}})$  index. The excess of activity could be an effect of the young age of the stars. Owing to the late spectral type of the stars, evolutionary models are unable to provide stringent constraints on their age. However, we calculated the Galactic space velocities (see Table 4) using the spectroscopic parallaxes reported in Hellier et al. (2011) and Bakos et al. (2011) for WASP-43 and HAT-P-20, respectively. Both stars have space velocities not compatible with any of the known nearby young moving groups (Zuckerman & Song 2004). We conclude that the origin of the enhanced activity is likely to be sought in the tidal and/or magnetic interactions of the stars with their close-in massive planetary companions.

## 5.2. Obliquity and stellar rotation

In Fig. 8, we revisited and updated the diagrams in Fig. 1 of Dawson (2014). Our diagrams also differ in that we did not apply the cuts in planet mass ( $M_{\text{pl}} > 0.5 M_J$ ) and period ( $P > 7$  days) used in Dawson (2014). We emphasise that all three stars studied in this work have  $T_{\text{eff}} \sim 4500$  K, hence they populate a region of the  $\lambda$ - $T_{\text{eff}}$  diagram that was largely unexplored before. Our three targets show small obliquities and, taking into consideration the relatively high mass and short orbital period of their planets, they appear consistent with the  $\lambda$ - $T_{\text{eff}}$  trend, according to which planets around stars with  $T_{\text{eff}} \lesssim 6250$  K have aligned orbits (Albrecht et al. 2012).

Dawson (2014) notices that for  $T_{\text{eff}} \leq 6000$  K, out of 19 systems with known  $\lambda$ , the two with the highest values of the projected stellar angular rotational velocity  $\Omega_* \sin I_*$  correspond to the most massive planets (CoRoT-2b and CoRoT-18b)<sup>5</sup>. She argues that this was the result of a planet mass dependence of the stellar projected rotation frequencies for cool stars, with massive planets being able to spin up their host stars via tidal interaction, contrasting the magnetic braking. She was able to reproduce this and other observational trends in a theoretical framework in which, for cool stars, the mass dependence was insensitive to the stellar  $T_{\text{eff}}$  (see right bottom diagram of her Fig. 1). However, our targets, in particular HAT-P-20 and Qatar-2, in spite of the large mass of the planets, have small values of  $\Omega_* \sin I_*$  (see the bottom panel of Fig. 8). This suggests that, probably, at the temperatures of our targets ( $T_{\text{eff}} \sim 4500$  K), the magnetic braking dominates over tidal spin up; a larger number of similar systems should be studied to settle this issue.

## 5.3. Tidal timescales

All our systems are not as yet synchronized, i.e., far from tidal equilibrium. In principle, only HAT-P-20 could reach a stable equilibrium because its total angular momentum is very close to the minimum value required according to Hut (1980) while, for WASP-43 and Qatar-2, it is smaller by a factor of about two. However, given the steady angular momentum loss produced by the magnetized wind in late-type stars, this type of stable equilibrium, even if established, cannot be maintained in HAT-P-20 (Damiani & Lanza 2015). Since the orbital periods of the three systems are shorter than the rotation periods, tides transfer angular momentum from the orbit to the stellar spin and the fate of these close-in planets is to fall towards their host stars.

An estimate of the infall timescale in our systems is made very uncertain by our ignorance of the physics of the dissipation of tidal kinetic energy inside late-type stars and planets, in particular in relation to the dissipation of dynamical tides, i.e., the wave-like perturbations excited by the tidal potential that varies periodically in the reference frame of the stars and planets (Ogilvie 2014). We parameterize the efficiency of tidal dissipation by means of the so-called modified tidal quality factors,  $Q'_s$  and  $Q'_p$  for the star and the planet, respectively. In close binary systems that consist of two late-type stars, the observations suggest  $Q'_s \approx 10^6$  (Ogilvie & Lin 2007), which would imply a short remaining lifetime for all our three systems, ranging from  $\sim 13$  Myr for WASP-43 to  $\sim 900$  Myr for HAT-P-20 (from Eq. (1) in Metzger et al. 2012). The e-folding timescale for the decrease of any initial obliquity of our systems would be comparable or shorter, ranging from  $\sim 10$  Myr for WASP-43 to

<sup>5</sup> The third massive planet shown in Fig. 8 is HD 80606b: with an orbital period of  $\sim 111$  days, it is not expected to have any significant tidal interactions with its host star.

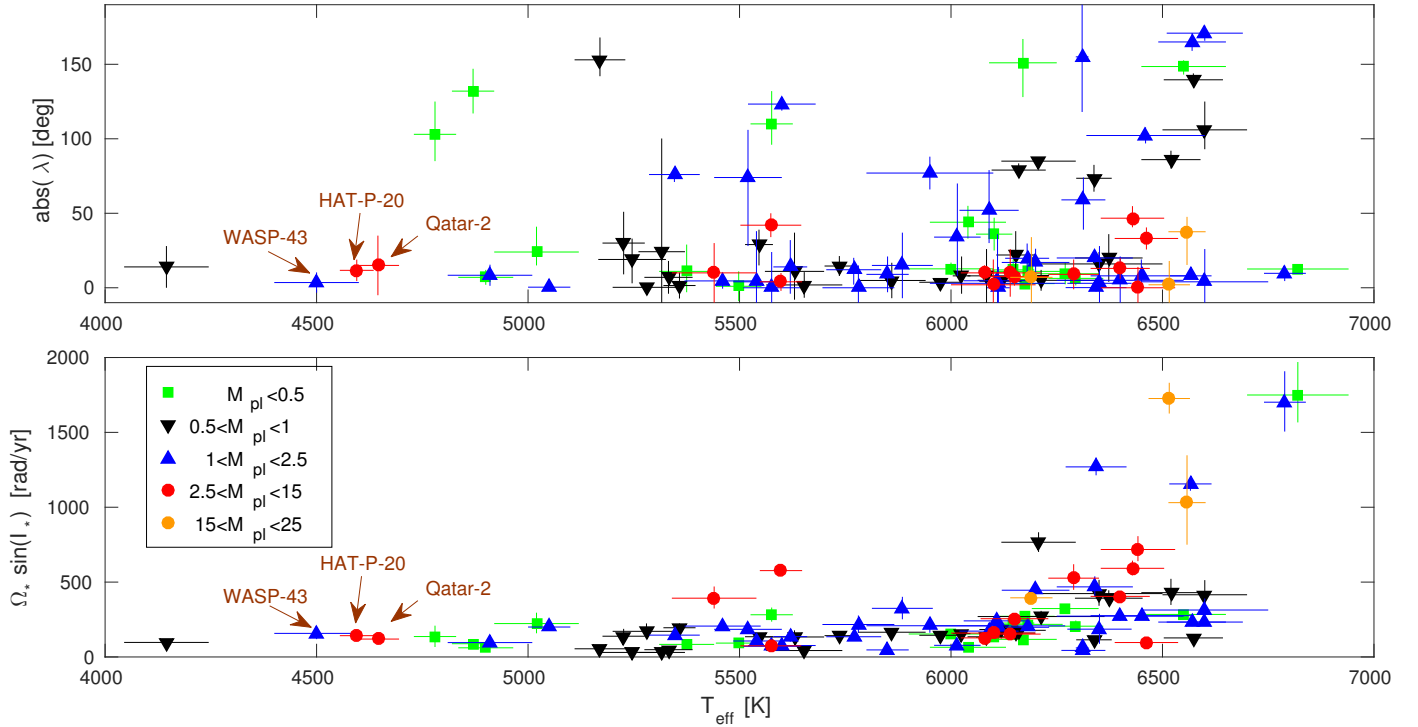


**Fig. 8.** *Top panel:*  $\lambda$ - $T_{\text{eff}}$  diagram for all the transiting planets with published determinations of  $\lambda$ . Only two systems with  $T_{\text{eff}} > 7000$  K were not included. *Bottom panel:* projected stellar angular rotational velocity  $\Omega_* \sin(i_*)$  as a function of the stellar  $T_{\text{eff}}$ . We referred to the <http://www.astro.keele.ac.uk/jkt/tepcat/> website for the values of  $\lambda$ ,  $T_{\text{eff}}$ ,  $R_*$  and  $M_{\text{pl}}$ ; the values of  $V \sin i_*$  were compiled by exploring the literature.

160 Myr for HAT-P-20, if we adopt the constant time-lag model of [Leconte et al. \(2010\)](#) and the presently measured parameters of the systems (see Table 4)<sup>6</sup>.

An observational lower limit  $Q'_s \gtrsim 10^5$  for WASP-43 was obtained by [Hoyer et al. \(2016\)](#), but it is far too low to be useful in our context. Assuming a likely tidal spin-up of the host star in the HATS-18 system, [Penev et al. \(2016\)](#) estimate  $Q'_s$  for that solar-like host. Scaling their value according to the different rotation periods of our target host stars based on the inertial wave dissipation model by [Ogilvie & Lin \(2007\)](#), we assume  $Q'_s = 10^7$ , while  $Q'_p = 10^6$  is appropriate for WASP-43 b and Qatar-2 b, and  $Q'_p = 5 \times 10^6$  for HAT-P-20 b in view of its longer period, by scaling from the value of  $Q'_p \approx 10^5$  for Jupiter (see, Sect. 5.4 in [Ogilvie 2014](#)). Also a  $Q'_s \sim 10^7$  is in general agreement with the statistical study by [Jackson et al. \(2009\)](#). With these values of the modified tidal quality factors, we obtain remaining lifetimes ranging from  $\sim 130$  Myr for WASP-43 to  $\sim 9$  Gyr for HAT-P-20. The expected O-C of the epoch of mid-transit with respect to a constant-period ephemeris is the largest for WASP-43 and it is of  $\sim 5.5$  s in ten years. The e-folding decay time of the initial obliquity ranges from  $\sim 100$  Myr for WASP-43 to  $\sim 1.6$  Gyr for HAT-P-20, i.e., shorter than the probable ages of the systems, thus suggesting that tides could have had enough time to align any initially oblique spin of the stars. On the other hand, the dissipation of any initial orbital eccentricity is dominated by the tides inside the planets and the corresponding e-folding timescales are shorter than  $\sim 10$  Myr for WASP-43 and Qatar-2, while this is of  $\sim 4$  Gyr in the case of HAT-P-20, suggesting that its present

non-zero eccentricity could have been excited when the system formed.

As mentioned in Sect. 2.2, HAT-P-20 has a visual companion at an angular separation of 6.9 arcsec. In the URAT catalog ([Nicholson 2015](#); [Zacharias et al. 2015](#)), HAT-P-20 and its companion are reported to have a common proper motion, separation  $\rho = 6.93$  arcsec and position angle  $\text{PA} = 320.6$  deg at the epoch  $\text{TE} = 2013.865$  yr. Previous observations indicated similar values:  $\rho = 6.939$  arcsec,  $\text{PA} = 320.6$  deg,  $\text{TE} = 2001.068$  yr ([Hartkopf et al. 2013](#));  $\rho = 6.860$  arcsec,  $\text{PA} = 320.3$  deg,  $\text{TE} = 1998.07$  yr ([Wycoff et al. 2006](#)). Thus, in all probability the two stars are physical companions; at an estimated distance of  $70 \pm 3$  pc ([Bakos et al. 2011](#)), the two stars have a projected separation of  $\sim 490$  AU. The stellar companion, based on its 2-MASS colors, is an M-dwarf ([Salz et al. 2015](#)). It cannot be excluded that gravitational perturbations from the companion played a role in the orbital evolution of HAT-P-20 b, which led to the current slightly eccentric and misaligned orbit.

## 6. Conclusions

We have measured the RM effect for the close-in and massive transiting planets orbiting WASP-43, HAT-P-20, and Qatar-2, three K-dwarf stars with effective temperatures of 4500, 4595, and 4640 K, respectively. We have found that the true spin-orbit angle  $\Psi$  of WASP-43 b is consistent with zero. For Qatar-2 b, we only report a marginal detection of the RM effect, however our results support previous evidence that the system is aligned. HAT-P-20 b, the one out of the three with the largest semi-major axis, has small but significant eccentricity ( $e = 0.0172 \pm 0.0016$ ) and obliquity ( $\Psi = 36^{+10}_{-12}$  deg), which might be related to the presence of the stellar companion at projected separation of  $\sim 490$  AU.

<sup>6</sup> We computed the constant time lag  $\tau$  using Eqs. (18) and (19) in [Leconte et al. \(2010\)](#) and assuming that the planet rotation is synchronous with the orbit.



HAT-P-20 and WASP-43, for which we could obtain reliable measurements of the average  $R'_{\text{HK}}$  index, show an activity level that exceeds the values typical for stars with the same rotation period. We take this as a likely manifestation of either tidal or magnetic star-planet interactions. A larger number of spectra with higher S/N would be needed to study the  $R'_{\text{HK}}$  variability and possible modulations with the planet orbital phase.

Contrary to what has been observed in two stars with  $T_{\text{eff}} \sim 5500$  K hosting massive planets, our targets do not show clear evidence of stellar rotational spin-up.

Overall, our findings are consistent with the scenario in which star-planet interactions have been effective in circularizing and aligning the planetary orbits, which is similar to what has already been observed for hotter stars up to  $T_{\text{eff}} \sim 6250$  K.

**Acknowledgements.** We thank the anonymous referee for her/his useful comments and suggestions. The GAPS project in Italy acknowledges the support by INAF through the Progetti Premiali funding scheme of the Italian Ministry of Education, University, and Research. Based on observations collected at Copernico telescope (Asiago, Italy) of the INAF–Osservatorio Astronomico di Padova. V. N. acknowledges partial support by the Università di Padova through the Studio preparatorio per il Plato Input Catalog grant (#2877-4/12/15) funded by the ASI-INAF agreement (No. 2015-019-R.0). The authors acknowledge Dr J. M. Alcalá, Dr. L. Bedin and Dr. G. Lodato for their comments and suggestions.

## References

- Albrecht, S., Winn, J. N., Johnson, J. A., et al. 2012, *ApJ*, **757**, 18
- Bakos, G. Á., Hartman, J., Torres, G., et al. 2011, *ApJ*, **742**, 116
- Ballerini, P., Micela, G., Lanza, A. F., & Pagano, I. 2012, *A&A*, **539**, A140
- Baluev, R. V., & Shaidulin, V. S. 2015, *MNRAS*, **454**, 4379
- Baranne, A., Queloz, D., Mayor, M., et al. 1996, *A&AS*, **119**, 373
- Barnes, J. W., Linscott, E., & Shporer, A. 2011, *ApJS*, **197**, 10
- Baruteau, C., Crida, A., Paardekooper, S.-J., et al. 2014, *Protostars and Planets VI*, 667
- Bate, M. R., Lodato, G., & Pringle, J. E. 2010, *MNRAS*, **401**, 1505
- Batygin, K. 2012, *Nature*, **491**, 418
- Biazzo, K., D'Orazi, V., Desidera, S., et al. 2012, *MNRAS*, **427**, 2905
- Blecic, J., Harrington, J., Madhusudhan, N., et al. 2014, *ApJ*, **781**, 116
- Borsa, F., Scandariato, G., Rainer, M., et al. 2015, *A&A*, **578**, A64
- Borucki, W. J. 2016, *Rep. Progr. Phys.*, **79**, 036901
- Boué, G., Montalto, M., Boisse, I., Oshagh, M., & Santos, N. C. 2013, *A&A*, **550**, A53
- Bryan, M. L., Alsubai, K. A., Latham, D. W., et al. 2012, *ApJ*, **750**, 84
- Canto Martins, B. L., Das Chagas, M. L., Alves, S., et al. 2011, *A&A*, **530**, A73
- Chaplin, W. J., Sanchis-Ojeda, R., Campante, T. L., et al. 2013, *ApJ*, **766**, 101
- Chen, G., van Boekel, R., Wang, H., et al. 2014, *A&A*, **563**, A40
- Claret, A., & Bloemen, S. 2011, *A&A*, **529**, A75
- Cosentino, R., Lovis, C., Pepe, F., et al. 2012, in *SPIE Conf. Ser.*, **8446**, 1
- Cosentino, R., Lovis, C., Pepe, F., et al. 2014, in *SPIE Conf. Ser.*, **9147**, 8
- Coughlin, J. L., Mullally, F., Thompson, S. E., et al. 2016, *ApJS*, **224**, 12
- Covino, E., Esposito, M., Barbieri, M., et al. 2013, *A&A*, **554**, A28
- Cuntz, M., Saar, S. H., & Musielak, Z. E. 2000, *ApJ*, **533**, L151
- Cutri, R. M., Skrutskie, M. F., van Dyk, S., et al. 2003, *VizieR Online Data Catalog: II/246*
- Dai, F., Winn, J. N., Yu, L., & Albrecht, S. 2017, *AJ*, **153**, 40
- Damasso, M., Biazzo, K., Bonomo, A. S., et al. 2015a, *A&A*, **575**, A111
- Damasso, M., Esposito, M., Nascimbeni, V., et al. 2015b, *A&A*, **581**, L6
- Damiani, C., & Lanza, A. F. 2015, *A&A*, **574**, A39
- Dawson, R. I. 2014, *ApJ*, **790**, L31
- Dawson, R. I., & Murray-Clay, R. A. 2013, *ApJ*, **767**, L24
- Demarque, P., Woo, J.-H., Kim, Y.-C., & Yi, S. K. 2004, *ApJS*, **155**, 667
- Deming, D., Knutson, H., Kammer, J., et al. 2015, *ApJ*, **805**, 132
- Desidera, S., Sozzetti, A., Bonomo, A. S., et al. 2013, *A&A*, **554**, A29
- D'Orazi, V., Biazzo, K., & Randich, S. 2011, *A&A*, **526**, A103
- Eastman, J., Siverd, R., & Gaudi, B. S. 2010, *PASP*, **122**, 935
- Esposito, M., Covino, E., Mancini, L., et al. 2014, *A&A*, **564**, L13
- Fabrycky, D. C., Lissauer, J. J., Ragozzine, D., et al. 2014, *ApJ*, **790**, 146
- Flower, P. J. 1996, *ApJ*, **469**, 355
- Gillon, M., Triaud, A. H. M. J., Fortney, J. J., et al. 2012, *A&A*, **542**, A4
- Giménez, A. 2006, *ApJ*, **650**, 408
- Granata, V., Nascimbeni, V., Piovato, G., et al. 2014, *Astron. Nachr.*, **335**, 797
- Hartkopf, W. I., Mason, B. D., Finch, C. T., et al. 2013, *AJ*, **146**, 76
- Hellier, C., Anderson, D. R., Collier Cameron, A., et al. 2011, *A&A*, **535**, L7
- Henden, A. A., Templeton, M., Terrell, D., et al. 2016, *VizieR Online Data Catalog: II/336*
- Hirano, T., Suto, Y., Taruya, A., et al. 2010, *ApJ*, **709**, 458
- Hoyer, S., Pallé, E., Dragomir, D., & Murgas, F. 2016, *AJ*, **151**, 137
- Hut, P. 1980, *A&A*, **92**, 167
- Jackson, B., Barnes, R., & Greenberg, R. 2009, *ApJ*, **698**, 1357
- Jiang, I.-G., Lai, C.-Y., Savushkin, A., et al. 2016, *AJ*, **151**, 17
- Knutson, H. A., Fulton, B. J., Montet, B. T., et al. 2014, *ApJ*, **785**, 126
- Krejčová, T., & Budaj, J. 2012, *A&A*, **540**, A82
- Lai, D. 2012, *MNRAS*, **423**, 486
- Lanza, A. F. 2008, *A&A*, **487**, 1163
- Lanza, A. F. 2012, *A&A*, **544**, A23
- Leconte, J., Chabrier, G., Baraffe, I., & Levrard, B. 2010, *A&A*, **516**, A64
- Lin, D. N. C., Bodenheimer, P., & Richardson, D. C. 1996, *Nature*, **380**, 606
- Lissauer, J. J., Ragozzine, D., Fabrycky, D. C., et al. 2011, *ApJS*, **197**, 8
- Lovis, C., & Pepe, F. 2007, *A&A*, **468**, 1115
- Lovis, C., Dumusque, X., Santos, N. C., et al. 2011, ArXiv e-print [[arXiv:1107.5325](https://arxiv.org/abs/1107.5325)]
- Maggio, A., Pillitteri, I., Scandariato, G., et al. 2015, *ApJ*, **811**, L2
- Malavolta, L., Nascimbeni, V., Piovato, G., et al. 2016, *A&A*, **588**, A118
- Mamajek, E. E., & Hillenbrand, L. A. 2008, *ApJ*, **687**, 1264
- Mancini, L., Southworth, J., Ciceri, S., et al. 2014, *MNRAS*, **443**, 2391
- Mancini, L., Esposito, M., Covino, E., et al. 2015, *A&A*, **579**, A136
- Mazeh, T., Perets, H. B., McQuillan, A., & Goldstein, E. S. 2015, *ApJ*, **801**, 3
- McLaughlin, D. B. 1924, *ApJ*, 60
- Metzger, B. D., Giannios, D., & Spiegel, D. S. 2012, *MNRAS*, **425**, 2778
- Morton, T. D., & Winn, J. N. 2014, *ApJ*, **796**, 47
- Močnik, T., Southworth, J., & Hellier, C. 2016, *MNRAS*, submitted [[arXiv:1608.07524](https://arxiv.org/abs/1608.07524)]
- Nascimbeni, V., Piovato, G., Bedin, L. R., & Damasso, M. 2011, *A&A*, **527**, A85
- Nascimbeni, V., Cunial, A., Murabito, S., et al. 2013, *A&A*, **549**, A30
- Nicholson, M. P. 2015, *VizieR Online Data Catalog: I/330*
- Noyes, R. W., Hartmann, L. W., Baliunas, S. L., Duncan, D. K., & Vaughan, A. H. 1984, *ApJ*, **279**, 763
- Ogilvie, G. I. 2014, *ARA&A*, **52**, 171
- Ogilvie, G. I., & Lin, D. N. C. 2007, *ApJ*, **661**, 1180
- Ohta, Y., Taruya, A., & Suto, Y. 2005, *ApJ*, **622**, 1118
- Penev, K. M., Hartman, J. D., Bakos, G. A., et al. 2016, *AJ*, **152**, 127
- Pepe, F., Mayor, M., Galland, F., et al. 2002, *A&A*, **388**, 632
- Poppenhaeger, K., Roßbrade, J., & Schmitt, J. H. M. M. 2010, *A&A*, **515**, A98
- Poretti, E., Boccato, C., Claudi, R., et al. 2016, *Mem. Soc. Astron. Italiana*, **87**, 141
- Queloz, D., Eggenberger, A., Mayor, M., et al. 2000, *A&A*, **359**, L13
- Ricci, D., Ramón-Fox, F. G., Ayala-Loera, C., et al. 2015, *PASP*, **127**, 143
- Rogers, T. M., Lin, D. N. C., & Lau, H. H. B. 2012, *ApJ*, **758**, L6
- Rossiter, R. A. 1924, *ApJ*, 60
- Salz, M., Schneider, P. C., Czesla, S., & Schmitt, J. H. M. M. 2015, *A&A*, **576**, A42
- Sanchis-Ojeda, R., & Winn, J. N. 2011, *ApJ*, **743**, 61
- Schlaufman, K. C. 2010, *ApJ*, **719**, 602
- Shkolnik, E. L. 2013, *ApJ*, **766**, 9
- Smareglia, R., Bignamini, A., Knapic, C., Molinaro, M., & GAPS Collaboration 2014, in *Astronomical Data Analysis Software and Systems XXIII*, eds. N. Manset, & P. Forshay, *ASP Conf. Ser.*, **485**, 435
- Snedden, C. 1973, *ApJ*, **184**, 839
- Southworth, J. 2011, *MNRAS*, **417**, 2166
- Southworth, J., Hinse, T. C., Jørgensen, U. G., et al. 2009, *MNRAS*, **396**, 1023
- Southworth, J., Hinse, T. C., Burgdorf, M., et al. 2014, *MNRAS*, **444**, 776
- Sozzetti, A., Torres, G., Charbonneau, D., et al. 2007, *ApJ*, **664**, 1190
- Suárez Mascareño, A., Rebolo, R., González Hernández, J. I., & Esposito, M. 2015, *MNRAS*, **452**, 2745
- Thies, I., Kroupa, P., Goodwin, S. P., Stamatellos, D., & Whitworth, A. P. 2011, *MNRAS*, **417**, 1817
- Triaud, A. H. M. J., Gillon, M., Ehrenreich, D., et al. 2015, *MNRAS*, **450**, 2279
- Valenti, J. A., & Fischer, D. A. 2005, *ApJS*, **159**, 141
- Winn, J. N., Holman, M. J., Henry, G. W., et al. 2007, *AJ*, **133**, 1828
- Winn, J. N., Fabrycky, D., Albrecht, S., & Johnson, J. A. 2010a, *ApJ*, **718**, L145
- Winn, J. N., Johnson, J. A., Howard, A. W., et al. 2010b, *ApJ*, **723**, L223
- Wöllert, M., & Brandner, W. 2015, *A&A*, **579**, A129
- Wu, Y., & Lithwick, Y. 2011, *ApJ*, **735**, 109
- Wycoff, G. L., Mason, B. D., & Urban, S. E. 2006, *AJ*, **132**, 50
- Zacharias, N., Finch, C., Subasavage, J., et al. 2015, *AJ*, **150**, 101
- Zuckerman, B., & Song, I. 2004, *ARA&A*, **42**, 685

- 
- <sup>1</sup> INAF–Osservatorio Astronomico di Capodimonte, via Moiariello, 16, 80131 Naples, Italy  
e-mail: mesposito@na.astro.it
- <sup>2</sup> INAF–Osservatorio Astronomico di Padova, Vicolo dell’Osservatorio 5, 35122 Padova, Italy
- <sup>3</sup> Max-Planck-Institut für Astronomie, Königstuhl 17, 69117 Heidelberg, Germany
- <sup>4</sup> INAF–Osservatorio Astrofisico di Catania, via S. Sofia 78, 95123 Catania, Italy
- <sup>5</sup> Astrophysics Group, Keele University, Staffordshire, ST5 5BG, UK
- <sup>6</sup> INAF–Osservatorio Astrofisico di Torino, via Osservatorio 20, 10025, Pino Torinese, Italy
- <sup>7</sup> Instituto de Astrofísica de Canarias, C/ vía Láctea, s/n, 38205 La Laguna (Tenerife), Spain
- <sup>8</sup> Departamento de Astrofísica, Universidad de La Laguna, Avda. Astrofísico Francisco Sánchez, s/n, 38206 La Laguna (TF), Spain
- <sup>9</sup> INAF–Osservatorio Astronomico di Palermo, Piazza del Parlamento, 1, 90134 Palermo, Italy
- <sup>10</sup> Dipartimento di Fisica e Astronomia Galileo Galilei – Università di Padova, Vicolo dell’Osservatorio 2, 35122 Padova, Italy
- <sup>11</sup> INAF–Fundación Galileo Galilei, Rambla José Ana Fernandez Pérez 7, 38712 Breña Baja, Spain
- <sup>12</sup> INAF–Osservatorio Astronomico di Brera, via E. Bianchi 46, 23807 Merate (LC), Italy
- <sup>13</sup> INAF–Osservatorio Astronomico di Trieste, via G. B. Tiepolo 11, 34143 Trieste, Italy
- <sup>14</sup> INAF–IASF Milano, via Bassini 15, 20133 Milano, Italy
- <sup>15</sup> INAF–Osservatorio Astronomico di Roma, via Frascati 33, 00040 Monte Porzio Catone (Roma), Italy
- <sup>16</sup> Dipartimento di Fisica, Università di Roma Tor Vergata, via della Ricerca Scientifica 1, 00133 Roma, Italy

## Appendix A: RV tables

Table A.1. HARPS-N RV data for WASP-43.

BJD (TDB)	$T_{\text{exp}}$ [s]	RV [km s <sup>-1</sup> ]	Error [km s <sup>-1</sup> ]	$FWHM$ [km s <sup>-1</sup> ]	Bis. span [km s <sup>-1</sup> ]	Air mass	Flag
2 456 363.415882	450	-3.2736	0.0111	7.17	0.086	1.59	o
2 456 363.421396	450	-3.3145	0.0120	7.15	0.076	1.55	o
2 456 363.426923	450	-3.3185	0.0115	7.16	0.027	1.51	o
2 456 363.432437	450	-3.3278	0.0096	7.18	0.015	1.48	o
2 456 363.437951	450	-3.3683	0.0093	7.14	0.060	1.45	o
2 456 363.443460	450	-3.3820	0.0091	7.16	0.056	1.42	o
2 456 363.448974	450	-3.4072	0.0092	7.25	0.046	1.40	o
2 456 363.454484	450	-3.4373	0.0093	7.16	0.056	1.38	o
2 456 363.459988	450	-3.4560	0.0088	7.17	0.057	1.36	o
2 456 363.465502	450	-3.4526	0.0095	7.16	0.102	1.34	i
2 456 363.471016	450	-3.5011	0.0099	7.12	0.034	1.33	i
2 456 363.476525	450	-3.4876	0.0096	7.16	0.079	1.31	i
2 456 363.482039	450	-3.5192	0.0096	7.20	0.057	1.30	i
2 456 363.487549	450	-3.5517	0.0094	7.19	0.057	1.29	i
2 456 363.493054	450	-3.5978	0.0093	7.17	0.080	1.29	i
2 456 363.498567	450	-3.6221	0.0102	7.14	0.024	1.28	i
2 456 363.504081	450	-3.6596	0.0091	7.15	0.071	1.28	i
2 456 363.509590	450	-3.6773	0.0086	7.14	0.023	1.28	i
2 456 363.515104	450	-3.6747	0.0090	7.19	0.060	1.28	i
2 456 363.520614	450	-3.6976	0.0097	7.23	0.005	1.28	o
2 456 363.526123	450	-3.7218	0.0103	7.18	0.032	1.28	o
2 456 363.531624	450	-3.7571	0.0109	7.22	0.025	1.29	o
2 456 363.537128	450	-3.7764	0.0113	7.17	0.043	1.30	o
2 456 363.542642	450	-3.7869	0.0104	7.13	0.062	1.30	o
2 456 363.548156	450	-3.8216	0.0113	7.21	0.050	1.31	o
2 456 363.553670	450	-3.8339	0.0132	7.18	0.076	1.33	o
2 456 363.559179	450	-3.8659	0.0117	7.16	0.073	1.34	o
2 456 363.564693	450	-3.8770	0.0154	7.22	0.106	1.36	o
2 456 363.571207	450	-3.8913	0.0144	7.26	0.083	1.38	o
2 456 363.576712	450	-3.9012	0.0121	7.18	0.068	1.40	o
2 456 363.582230	450	-3.9561	0.0163	7.17	0.082	1.43	o
2 456 363.587740	450	-3.9589	0.0127	7.15	0.048	1.46	o
2 456 376.517002	900	-3.6434	0.0058	7.27	0.034	1.33	i
2 456 377.589657	900	-4.1247	0.0088	7.40	-0.093	1.81	o
2 456 381.558437	450	-4.0933	0.0088	7.19	0.072	1.59	o
2 456 381.563762	450	-4.1130	0.0089	7.18	0.030	1.64	o
2 456 382.512779	900	-3.9513	0.0052	7.20	0.041	1.37	o
2 457 050.557137	900	-3.2261	0.0192	7.18	0.101	1.43	o
2 457 116.447829	900	-3.2458	0.0045	7.11	0.075	1.28	o
2 457 145.424807	900	-4.1267	0.0154	7.02	0.052	1.38	o

**Notes.** The columns report: BJD (TDB), the mid-exposure barycentric Julian dates in barycentric dynamical time;  $T_{\text{exp}}$ , the exposure time; RV and error are the radial velocity measurement and its estimated uncertainty;  $FWHM$ , the full width at half maximum of the cross-correlation function; Bis. span, the radial velocity bisector span of the CCF; Air mass, the air mass of the star at the beginning of the exposure; Flag, indicating whether the spectrum was taken in-transit (i) or off-transit (o).

**Table A.2.** HARPS-N RV data for HAT-P-20.

BJD (TDB)	$T_{\text{exp}}$ [s]	RV [km s <sup>-1</sup> ]	Error [km s <sup>-1</sup> ]	$FWHM$ [km s <sup>-1</sup> ]	Bis. span [km s <sup>-1</sup> ]	Air mass	†
2 456 252.743420	900	-17.8116	0.0034	7.02	0.073	1.05	o
2 456 305.646766	900	-17.6177	0.0030	7.01	0.039	1.17	o
2 456 323.675026	900	-19.2777	0.0082	7.12	0.046	1.79	o
2 456 569.727872	900	-16.8530	0.0031	7.03	0.055	1.15	o
2 456 581.752206	900	-17.8062	0.0026	7.05	0.050	1.02	o
2 456 606.758475	1200	-16.9772	0.0039	7.08	0.026	1.03	o
2 456 608.768700	900	-19.0709	0.0025	7.10	0.064	1.05	o
2 456 608.778237	400	-19.0600	0.0045	7.10	0.057	1.06	o
2 456 609.779656	900	-16.8533	0.0056	7.06	0.050	1.08	o
2 456 621.746725	1200	-17.1818	0.0030	7.12	0.036	1.08	o
2 456 622.723432	900	-19.3090	0.0035	7.12	0.056	1.03	o
2 456 631.627655	900	-19.2637	0.0024	7.01	0.068	1.01	o
2 456 719.481675	900	-17.1670	0.0063	7.11	0.054	1.08	o
2 456 723.544801	900	-19.2887	0.0036	7.10	0.048	1.43	o
2 456 728.410880	600	-17.8740	0.0046	7.05	0.009	1.01	o
2 456 728.418111	600	-17.8955	0.0046	7.08	0.027	1.01	o
2 456 728.425345	600	-17.9150	0.0046	7.07	0.017	1.02	o
2 456 728.432580	600	-17.9264	0.0046	7.09	0.013	1.03	o
2 456 728.439814	600	-17.9500	0.0050	7.09	-0.014	1.04	o
2 456 728.447035	600	-17.9705	0.0050	7.08	-0.001	1.06	i
2 456 728.454265	600	-17.9766	0.0046	7.09	0.016	1.07	i
2 456 728.461495	600	-17.9831	0.0044	7.06	0.005	1.09	i
2 456 728.468729	600	-18.0035	0.0041	7.07	0.033	1.11	i
2 456 728.475959	600	-18.0383	0.0046	7.07	0.023	1.13	i
2 456 728.483184	600	-18.0725	0.0048	7.08	0.030	1.16	i
2 456 728.490418	600	-18.0874	0.0057	7.07	0.030	1.18	i
2 456 728.497653	600	-18.1251	0.0062	7.12	0.011	1.22	i
2 456 728.504882	600	-18.1492	0.0052	7.07	0.027	1.25	i
2 456 728.512125	600	-18.1571	0.0052	7.06	0.015	1.29	i
2 456 728.519346	600	-18.1668	0.0054	7.08	0.010	1.33	i
2 456 728.526585	600	-18.1851	0.0056	7.05	0.009	1.38	o
2 456 728.533816	600	-18.2109	0.0054	7.06	0.033	1.44	o
2 456 728.541041	600	-18.2263	0.0065	7.16	-0.006	1.50	o
2 456 728.548267	600	-18.2480	0.0076	7.15	0.016	1.57	o
2 456 728.555489	600	-18.2684	0.0071	7.17	-0.008	1.65	o
2 456 728.562718	600	-18.2802	0.0079	7.20	0.005	1.75	o
2 456 728.569953	600	-18.3064	0.0091	7.16	-0.018	1.85	o
2 456 976.687433	900	-19.2139	0.0022	6.95	0.043	1.01	o
2 457 005.717112	900	-18.7385	0.0043	6.94	0.072	1.13	o
2 457 011.702769	900	-18.1656	0.0036	6.96	0.065	1.14	o
2 457 125.412095	900	-18.4303	0.0020	7.04	0.068	1.25	o
2 457 389.617073	900	-17.5685	0.0045	7.05	0.063	1.02	o

**Notes.** See the caption of Table A.1 for the meaning of the columns. <sup>(†)</sup> i ≡ in-transit, o ≡ out-of-transit.



**Table A.3.** HARPS-N RV data for Qatar-2.

BJD (TDB)	$T_{\text{exp}}$ [s]	RV [km s <sup>-1</sup> ]	Error [km s <sup>-1</sup> ]	$FWHM$ [km s <sup>-1</sup> ]	Bis. span [km s <sup>-1</sup> ]	Air mass	<sup>†</sup>
2 456 775.434193	900	-23.7480	0.0271	6.69	0.089	1.51	o
2 456 775.444895	900	-23.7285	0.0265	6.65	0.025	1.44	o
2 456 775.455598	900	-23.8385	0.0307	6.69	0.081	1.38	o
2 456 775.466305	900	-23.8248	0.0261	6.72	-0.004	1.34	o
2 456 775.477012	900	-23.8530	0.0253	6.75	0.089	1.30	o
2 456 775.487705	900	-23.8691	0.0305	6.73	-0.069	1.27	i
2 456 775.498412	900	-23.8725	0.0271	6.72	0.132	1.25	i
2 456 775.509114	900	-23.9181	0.0242	6.73	-0.011	1.24	i
2 456 775.519825	900	-23.9703	0.0254	6.60	0.038	1.23	i
2 456 775.530532	900	-24.0137	0.0225	6.74	-0.008	1.23	i
2 456 775.541239	900	-24.0664	0.0304	6.74	0.012	1.23	i
2 456 775.551946	900	-24.0915	0.0374	6.59	0.111	1.24	i
2 456 775.562648	900	-24.0793	0.0407	6.67	0.055	1.26	i
2 456 775.573355	900	-24.1343	0.0432	6.71	0.015	1.28	o
2 456 775.584062	900	-24.1286	0.0409	6.80	0.000	1.32	o
2 456 775.594760	900	-24.1363	0.0361	6.72	-0.030	1.35	o
2 456 775.605458	900	-24.2294	0.0386	6.69	0.052	1.40	o

**Notes.** See the caption of Table A.1 for the meaning of the columns. <sup>(†)</sup> i  $\equiv$  in-transit, o  $\equiv$  out-of-transit.